nature communications

Article

https://doi.org/10.1038/s41467-024-55430-4

Trigger inducible tertiary lymphoid structure formation using covalent organic frameworks for cancer immunotherapy

Received: 19 March 2024

Accepted: 11 December 2024

Published online: 02 January 2025

Check for updates

Liang Zhang[1,2,5], Boxin Zhang[1,5], Meng-Jie Zhang[1,5], Wenlang Li[2], Hao Li[1], Yantian Jiao[2], Qi-Chao Yang[1], Shuo Wang[1], Yuan-Tong Liu[1], An Song[1], Hai-Tao Feng[3], Jianwei Sun[2], Ryan T. K. Kwok[2], Jacky W. Y. Lam[2] ✉, Ben Zhong Tang[2,4] ✉ & Zhi-Jun Sun[1] ✉

The discovery of tertiary lymphoid structures (TLS) within tumor tissues provides a promising avenue to promote the efficacy of cancer immunotherapy. Yet, the lack of effective strategies to induce TLS formation poses a substantial obstacle. Thus, the exploration of potential inducers for TLS formation is of great interest but remains challenging. Here, inspired by the mechanism of artificially cultivated pearls, a covalent organic framework (COF) is employed to induce TLS formation. Single-cell sequencing analysis reveals that this is achieved by promotion of cytokine hypersecretion, which facilitates the maturation, proliferation, and migration of T and B cells, critical for triggering TLS formation. Furthermore, the efficacy of COF-mediated phototherapy in inducing TLS formation is validated in both the MC38 and 4MOSC1 female tumor models. Notably, a strong synergistic effect between COF-mediated phototherapy and αCTLA-4 is observed, resulting in the effective eradication of both primary and distant tumors, while also inhibiting tumor recurrence.

Immune checkpoint blockade (ICB) therapy has emerged as a promising and innovative therapeutic strategy for the treatment of cancer. Despite its considerable potential, the clinical efficacy of ICB is often impeded by a low response rate[1–6]. Recently, the identification of tertiary lymphoid structures (TLS) within the tumor immune microenvironment (TIME) has provided a powerful avenue for enhancing the response rate of ICB therapy[7–10]. These ectopic lymphoid organs, which develop in non-lymphoid chronic inflammation tissues such as hot tumors, have demonstrated the potential to augment the immune response by facilitating lymphocyte infiltration and antigen presentation[11,12]. Despite extensive research efforts dedicated to exploring the role of chemokines, cytokines, antibodies, and antigen-presenting cells in driving the formation of tumor-associated lymphoid structures, the number of effective nanomedicine-based TLS formation inducers reported so far remains limited[9,13–16]. Nanomedicines, such as metal-organic frameworks (MOFs) and covalent organic frameworks (COFs), have garnered considerable attention in cancer therapy owing to their excellent modifiability, targeting capability,

[1]State Key Laboratory of Oral & Maxillofacial Reconstruction and Regeneration, Key Laboratory of Oral Biomedicine Ministry of Education, Hubei Key Laboratory of Stomatology, School & Hospital of Stomatology, Frontier Science Center for Immunology and Metabolism, Taikang Center for Life and Medical Sciences, Wuhan University, Wuhan, China. [2]Division of Life Science and State Key Laboratory of Molecular Neuroscience, Department of Chemistry, The Hong Kong Branch of Chinese National Engineering Research Center for Tissue Restoration and Reconstruction, The Hong Kong University of Science and Technology, Clear Water Bay Kowloon, Hong Kong, China. [3]AIE Research Center, College of Chemistry and Chemical Engineering, Baoji University of Arts and Sciences, Baoji, Shanxi, China. [4]Shenzhen Institute of Aggregate Science and Technology, School of Science and Engineering, The Chinese University of Hong Kong, Shenzhen, Guangdong, China. [5]These authors contributed equally: Liang Zhang, Boxin Zhang, Meng-Jie Zhang. ✉e-mail: chjacky@ust.hk; tangbenz@cuhk.edu.cn; sunzj@whu.edu.cn

functionality, and immune evasion properties[17–23]. Nonetheless, the exploration of effective strategies harnessing MOFs or COFs to facilitate TLS formation remains largely unexplored. The formation of TLS usually necessitates a sustained inflammatory environment, akin to the prolonged period required for the formation of pearls following the implantation of a bead nucleus in artificial cultivation. Inspired by the mechanism of pearl cultivation, we hypothesize that COF-based nanomedicine may function similarly to the bead nucleus, owing to their outstanding performance in eliciting chronic inflammatory microenvironment which may ensure the successful formation of TLS and consequently promote the response rate of cancer immunotherapy. Given that these TLS are not naturally occurring but necessitate external intervention, we termed them as inducible TLS (iTLS).

TLS arises in the context of inflammatory conditions and is characterized by the structured aggregation of leukocytes and consists of an inner B cell zone interspersed with T cells[7]. Such structures bypass the need for dendritic cells and other immune cells to transport antigens to the lymph nodes to allow the direct binding between immune cells and cognate antigens within the TIME[11]. Moreover, the overexpression of inflammatory cytokines, including CXCL (10, 13, 19, 21), IL22, and IL7, within TLS can serve as a stimulus for the maturation and infiltration of immune cells, thereby potentiating the antitumor immune response[9,24]. As crystalline organic porous materials, COFs have demonstrated potential in cancer immunotherapy due to their good light absorption and biocompatibility[25–37]. However, the prospect of TLS induction by COF materials remains unexplored, primarily due to their constrained phototherapy performance, which inadequately stimulates a vigorous and sustained inflammatory response to elicit iTLS. In addition, traditional COF-based photosensitizers (PSs) are non-emissive and suffer from limited therapeutic efficacy due to the apoptosis resistance and aggregation-caused quenching (ACQ) effect in aggregate state, which reduce their capacity of reactive oxygen species (ROS) generation[38–40]. The utilization of aggregation-induced emission luminogens (AIEgens) based phototheranostic agents presents a promising strategy to address the ACQ issue, which shows enhanced ROS production upon aggregation[41–43]. Despite extensive efforts to incorporate AIEgens into COF skeletons have been put, the resulting COFs often show weak emission, due to the strong excited-state energy dissipation of the imine linkage[44–47].

In this study, a combination of electron-acceptor and π-bridge engineering strategy was employed to construct a series of high emissive AIE COF-based PSs, called TPDA-TDTA-COF, TPDA-BT-COF, and TPDA-ViBT-COF, with excellent photodynamic and photothermal therapy (PDT and PTT) performance. Among them, TPDA-ViBT-COF exhibited superior light absorption, appropriate band energy, high quantum yield, and long lifetime, making it a promising candidate for phototherapy. In vivo, studies revealed that TPDA-ViBT-COF-mediated phototherapy effectively ameliorated the immunosuppressive microenvironment while simultaneously stimulating the host defense system. This led to a vigorous and sustained inflammatory response, which was favorable for facilitating the formation of iTLS and boosting cancer immunotherapy (Fig. 1). Consequently, the high capability of COF-mediated phototherapy in inducing TLS formation was successfully validated in both the MC38 and 4MOSC1 tumor models. Notably, this therapeutic approach exhibited substantial efficacy in eliminating both primary and distant tumors, while also demonstrating an efficient inhibition of tumor recurrence.

Single cell RNA-sequence (scRNA-seq) has emerged as a powerful technique for investigating genetic and functional heterogeneity at the cellular level, enabling valuable insights into the tumor microenvironment and potential therapeutic strategies[48–51]. In our study, we employed a combination of scRNA-seq and enzyme-linked immunosorbent assay (ELISA) to comprehensively elucidate the mechanism underlying the formation of iTLS triggered by AIE COF-mediated phototherapy. The scRNA-seq analysis revealed a remarkable expansion of TLS-associated immune cells, including B cells and $CD4^+$ T cells, within neoplasms treated with TPDA-ViBT-COF. Additionally, multiplex immunohistochemistry (mIHC) results demonstrated extensive aggregates of leukocytes, characterized by an inner B cell zone surrounded by dispersed $CD4^+$ T cells, confirming the successful formation of iTLS upon TPDA-ViBT-COF treatment. Moreover, the ELISA results unveiled an over-secretion of CCL19, CCL21, CXCL10, IFNγ, TNFα, and IFNβ cytokines, known to promote T-cell congregation within the tumor microenvironment, as well as an overproduction of cytokines IL22, IL17, and IL13, recognized for enhancing B cell maturation, proliferation, and migration. Notably, the presence of TPDA-ViBT-COF within the iTLS along with extensive areas of CXCL13 positivity, indicated the ability of TPDA-ViBT-COF to promote the recruitment of systemic immune cells to the tumor, such as T and B cells. Collectively, these results suggest that TPDA-ViBT-COF-mediated phototherapy effectively induces iTLS formation by promoting the over-secretion of cytokines, thereby facilitating the recruitment, maturation, and proliferation of T and B cells.

In this work, we show that cytotoxic T-lymphocyte-associated protein 4 antibody (αCTLA-4) blockade is a more effective partner than programmed cell death protein 1 antibody (αPD-1) when combined with COF-mediated phototherapy. The synergistic effect of TPDA-ViBT-COF + αCTLA-4 effectively inhibits tumor recurrence and enhances survival, establishing COF-based iTLS inducers as a promising strategy for advancing cancer immunotherapy.

Results

Preparation and characterization of AIE COFs

AIE COFs were prepared by condensation of an tetra-amine, bis(4-aminophenyl)-[1,1′:2′,1″-terphenyl]-4,4″-diamine (1), with an tetra-aldehyde, ([1,1′-biphenyl]-4,4′-diylbis(azanetriyl))tetrabenzaldehyde (2), 4,4′,4″,4‴-((benzo[c][1,2,5]-thiadiazole-4,7-diylbis(4,1-phenylene)) bis(azanetriyl)) tetra-benzaldehyde (3), or ((((1E,1′E)-benzo[c][1,2,5]-thiadiazole-4,7-diylbis(ethene-2,1-diyl))bis(4,1-phenylene))bis-(azanetriyl))tetra-benzaldehyde (**4**) (Fig. 2a and Supplementary Figs. 1–6). These monomers (M-TPDA, M-TDTA, M-BT, and M-ViBT) exhibited the AIE characteristics: their emission in solvent/H_2O mixture was progressively increased with the increasing of H_2O fraction (Supplementary Fig. 7). To better identify the AIE COF structures, comprehensive spectroscopic studies were conducted. The structural characterization was accomplished through the Pawley refinement against their experimental small-angle X-ray scattering and powder X-ray diffraction (PXRD) data. Notably, the PXRD data originated from the eclipsed packing models exhibited a good concurrence with the experimental PXRD patterns of AIE COFs, as evidenced by the suitable calculated (*R*wp, *R*p) values, revealing their eclipsed packing structures (Fig. 2b, d, and Supplementary Tables. 1–4). The Brunauer-Emmett-Teller surface areas for these AIE COFs were identified as 1040 $m^2 g^{-1}$ for TPDA-TDTA-COF, 1230 $m^2 g^{-1}$ for TPDA-BT-COF, and 1610 $m^2 g^{-1}$ for TPDA-ViBT-COF, respectively (Fig. 2f and Supplementary Fig. 8). These AIE COFs was further identified by solid-state NMR, FT-IR, and X-ray photoelectron spectroscopy spectrum, which supporting the presence of imine linkages (Fig. 2e, g and Supplementary Fig. 9).

Photophysical properties of AIE COFs

The AIE PSs are underscored as a promising remedy for the ACQ effect, attributed to their resilience to high solution concentration, pronounced Stokes shift, and enhanced photostability in the aggregate state[52]. Moreover, the acceptor engineering strategy has validated its efficacy in augmenting the ROS generation ability of AIEgens by integrating a potent electron-accepting motif to conjugated chromophores to enable aggregation-induced intersystem crossing[53,54]. In this study, we utilized this acceptor engineering approach by integrating an electron-accepting functional group, (benzo[c][1,2,5]thiadiazole (BT)), into an AIE COF (TPDA-TDTA-COF) to construct TPDA-BT-COF,

https://doi.org/10.1038/s41467-024-55430-4

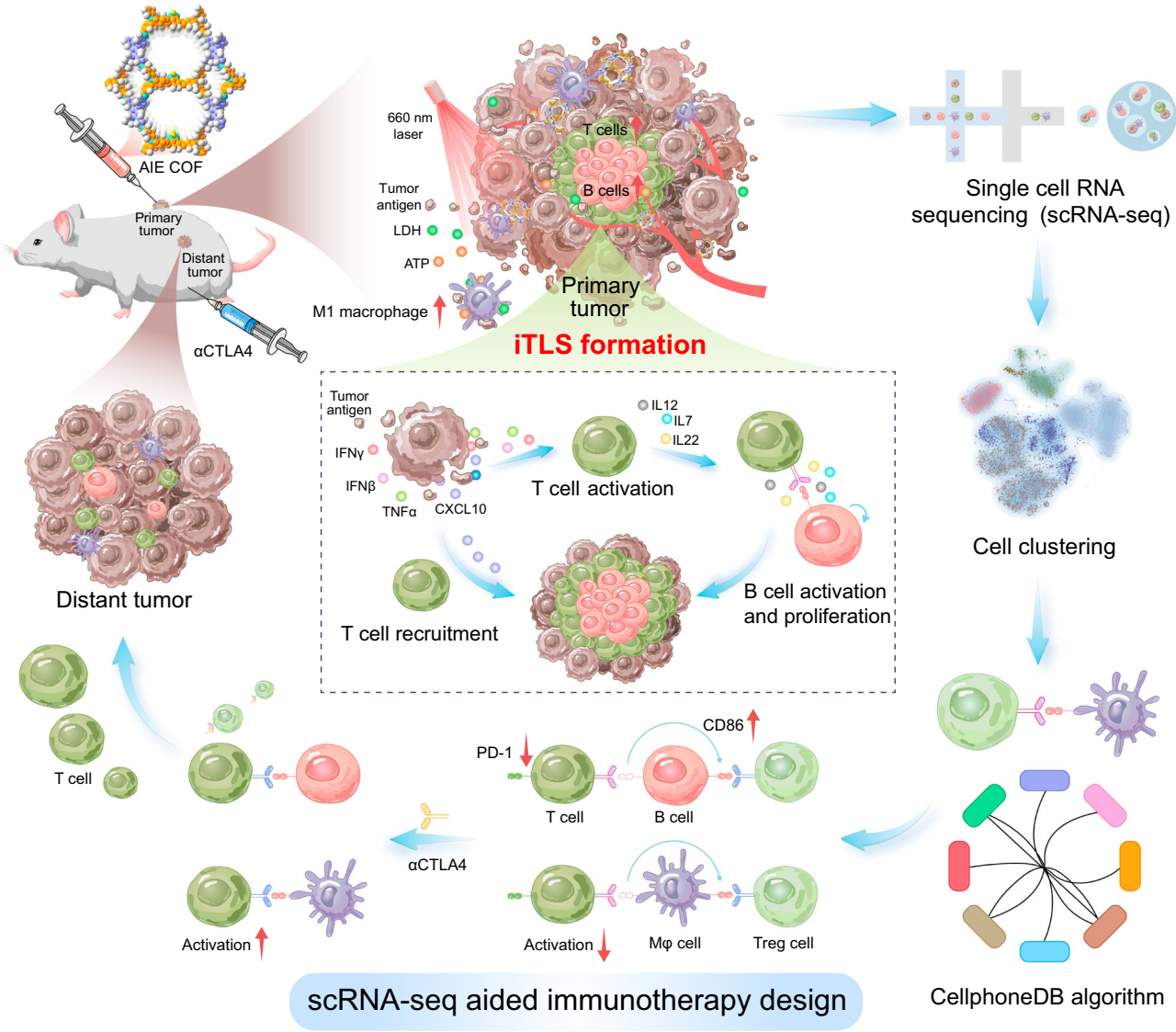

Fig. 1 | Illustration of the design of scRNA-seq aided immunotherapy facilitated by AIE COF-induced TLS formation. The application of AIE COF-mediated phototherapy leads to the induction of TLS formation by stimulating the excessive secretion of key cytokines. This process subsequently promotes the maturation, proliferation, and migration of T and B cells. To explore the underlying mechanisms, single-cell sequencing was utilized, and receptor-ligand interactions between cells were analyzed using CellphoneDB, a tool for characterizing cell-cell communication networks from scRNA-seq data. Notably, the analysis indicated that PD−1 expression in T cells did not increase following AIE COF treatment. In contrast, there of CD86 expression, a ligand for CTLA4 was markedly upregulated. Consequently, combining αCTLA4 blockade with AIE COF treatment exhibits a higher potential to effectively suppress the growth of both primary and distant tumors.

with a markedly improved ROS generation ability. π-bridge engineering strategy has been recognized as an effective method to heighten the PTT efficacy of AIEgens by incorporating molecular rotator motifs into conjugated chromophores to trigger molecular motion and increase the nonradioactive decay processes[55]. To further optimize the PTT effect of these AIE COFs, we utilized this strategy by incorporating a freely rotating vinyl group into TPDA-BT-COF to form another AIE COF, TPDA-ViBT-COF (Fig. 3a). Optical spectroscopy studies revealed that the BT-based COFs (TPDA-BT-COF and TPDA-ViBT-COF) exhibited distinctly redder absorption and emission than TPDA-TDTA-COF, unveiling the potency of the electron acceptor and π-bridge engineering strategy in augmenting the photophysical properties of AIE COFs (Fig. 3b–g). Among these AIE COFs, TPDA-ViBT-COF demonstrated stronger distinctly redder absorption and emission (Fig. 3b, d, and Supplementary Fig. 10), high quantum yield (Fig. 3f), long lifetime (Fig. 3g), and a narrowed bandgap (Fig. 3c, h and Supplementary data 1–3), both of which are critical for boosting the phototherapy performance. Thus, TPDA-ViBT-COF has the potential to serve as a promising candidate for phototherapy applications.

In vitro phototherapy efficacy of AIE COFs

Due to the good photophysical properties of TPDA-ViBT-COF, we investigated its potential as an AIE PS for PDT and PTT in vitro (Fig. 4a). 2,7-Dichlorodihydrofluorescein diacetate (DCFH) was utilized to assess the ROS production ability of TPDA-TDTA-COF, TPDA-BT-COF, and TPDA-ViBT-COF[56]. An obvious change in the fluorescence intensity of DCFH was observed upon the addition of TPDA-BT-COF or TPDA-ViBT-COF under 660 nm laser irradiation. In contrast, TPDA-TDTA-COF, without the BT unit, exhibited a moderate level of ROS generation capability (Fig. 4b, c). These results highlight the remarkable efficacy of the acceptor-engineering strategy employed by the BT unit in enhancing the PDT performance of TPDA-BT-COF and TPDA-ViBT-COF. In addition, these AIE COFs could generate heat upon laser irradiation. Among them, TPDA-ViBT-COF with freely rotating vinyl groups

https://doi.org/10.1038/s41467-024-55430-4

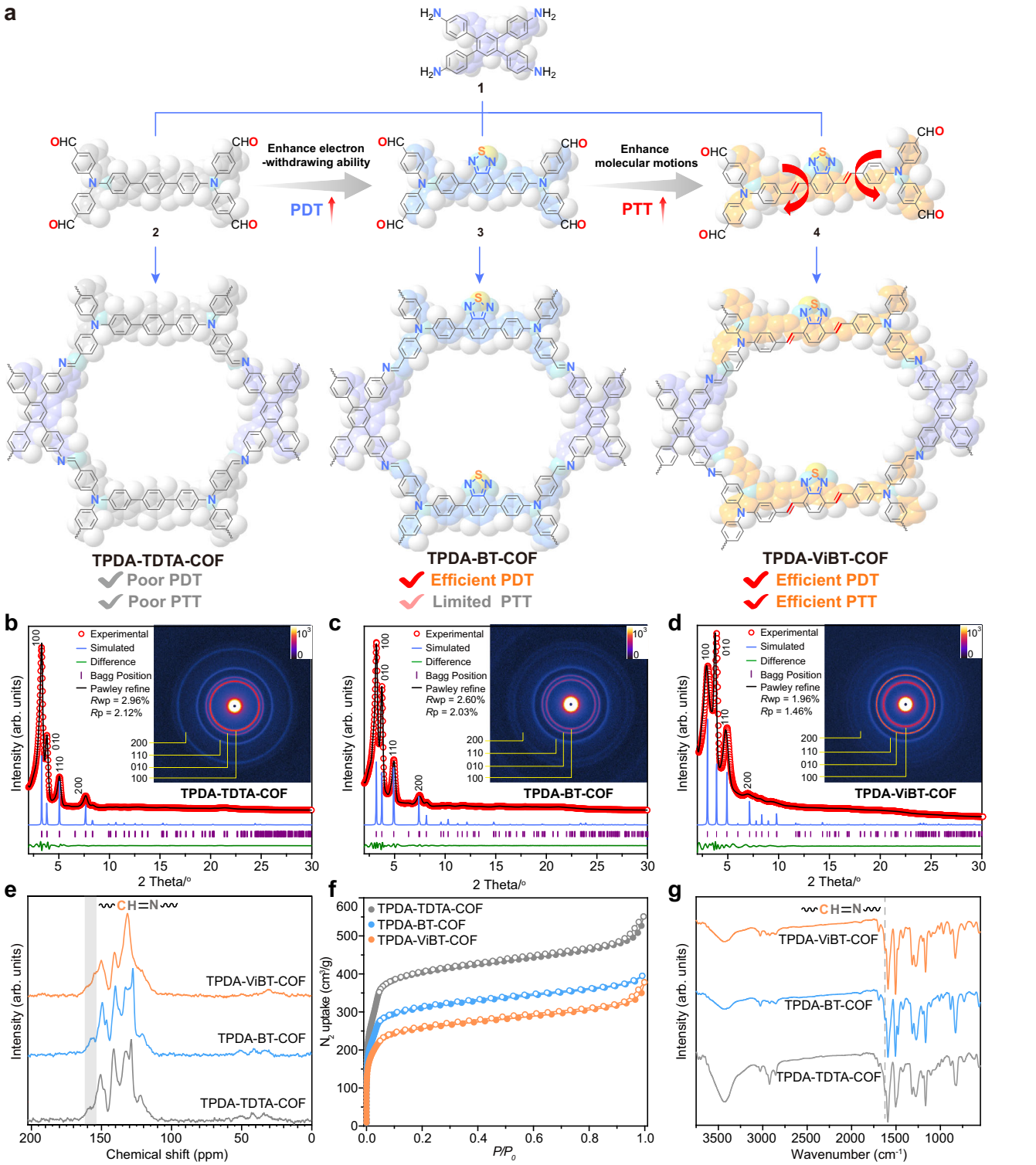

Fig. 2 | Characterization of TPDA-TDTA-COF, TPDA-BT-COF, and TPDA-ViBT-COF. a Synthesis route of TPDA-TDTA-COF, TPDA-BT-COF, and TPDA-ViBT-COF. **b**–**d** PXRD patterns of TPDA-TDTA-COF, TPDA-BT-COF, and TPDA-ViBT-COF; inserts: two dimensional small-angle X-ray scattering images of AIE COFs. **e**–**g** Solid-state NMR spectra, N_2 adsorption isotherms, and IR spectra of AIE COFs. PDT photodynamic therapy, PTT photothermal therapy. Source data are provided as a Source Data file.

showed better photothermal conversion ability due to its faster molecular motion (Fig. 4d, e). The good PTT effect of TPDA-ViBT-COF was further confirmed by the in vivo experimental results shown in Fig. 4f. Subsequently, the cytotoxicity of the AIE COFs was assessed by employing COF nanoparticles prepared through sonication treatment (Fig. 4g). On the other side, mouse-derived colon cancer cell line (MC38) was used to detect the phototherapy efficacy of TPDA-ViBT-COF. As demonstrated in Supplementary Fig. 11, the MC38 cells exhibited a clear red fluorescence signal after 12 h of co-culture, indicating that these AIE COFs were readily internalized by the cells. Subsequently, we further investigated the intracellular distribution of AIE COFs. Through confocal microscopy, we found that AIE COFs co-

https://doi.org/10.1038/s41467-024-55430-4

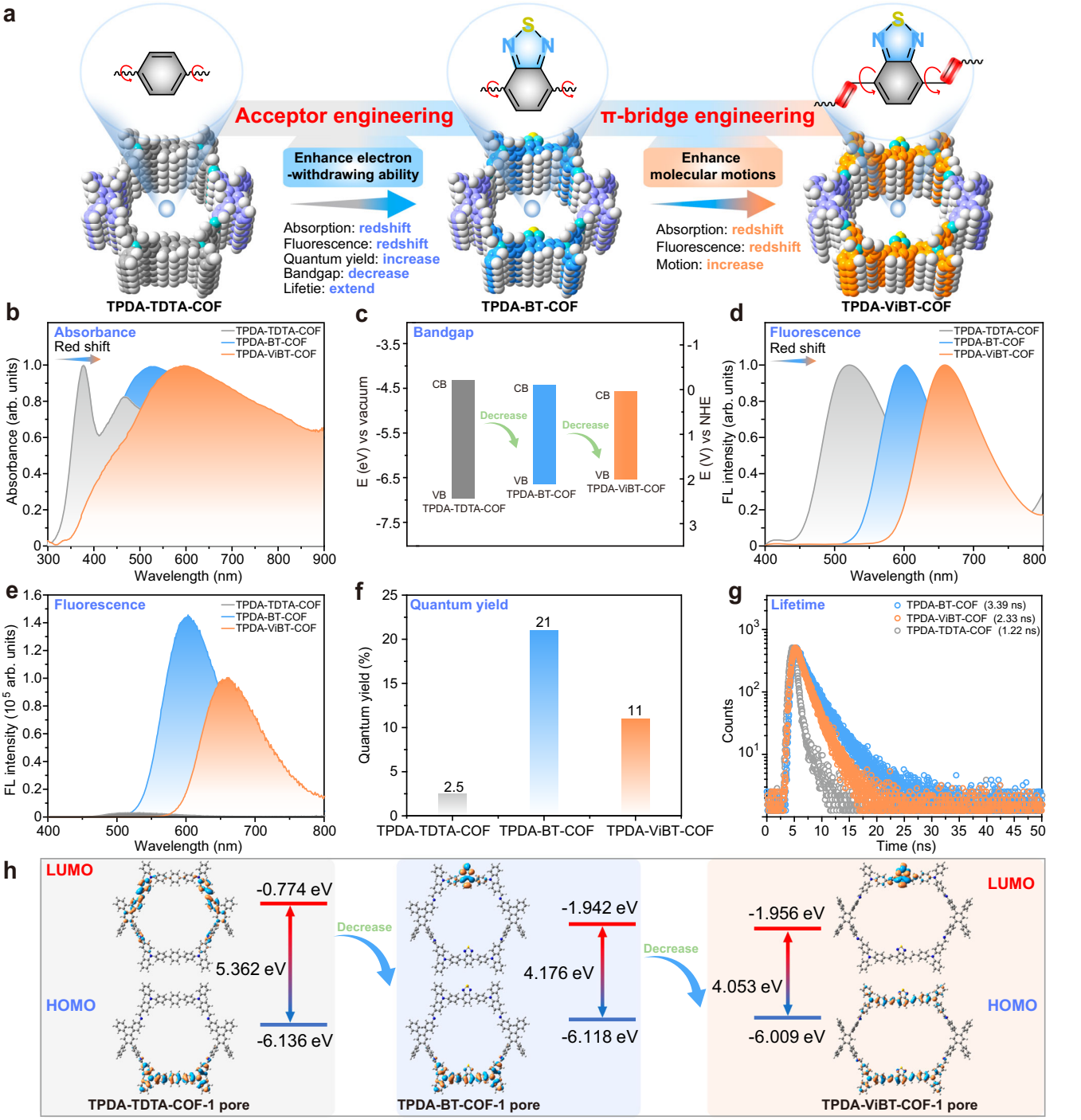

Fig. 3 | Photophysical properties of TPDA-TDTA-COF, TPDA-BT-COF, and TPDA-ViBT-COF. a Illustration of the advantages of TPDA-ViBT-COF. Ultraviolet-visible absorption spectra (**b**), band energy (**c**), solid-state photoluminescence (PL) spectra (**d**), steady-state PL spectra (**e**), quantum yield (**f**) and time-resolved PL spectra (**g**) of AIE COFs. **h** Density functional theory calculations of the bandgap of TPDA-TDTA-COF, TPDA-BT-COF, and TPDA-ViBT-COF, HOMO highest occupied molecular orbital, LUMO lowest unoccupied molecular orbital. Source data are provided as a Source Data file.

localized with lysosomes and endoplasmic reticulum, rather than mitochondria (Supplementary Figs. 12 and 32). The cell counting Kit-8 (CCK8) assay results displayed that in the absence of laser irradiation, over 80% of MC38 cells remained viable after exposure to COF solutions with varied concentrations, which indicated the good biocompatibility of these AIE COFs. (Fig. 4h). In contrast, less than 25% of MC38 cells survived after being subjected to TPDA-ViBT-COF upon laser irradiation. In comparison to MC38 cells, TPDA-ViBT-COF combined with laser irradiation exhibited lower toxicity to L929 and HOK cells (Fig. 4i and Supplementary Fig. 14). This reduced toxicity in non-tumor cells can be attributed to their lower baseline levels of ROS and more robust antioxidant defense systems, which enable them to better manage oxidative stress induced by phototherapy. However, cancer cells, like MC38, typically exhibit elevated ROS levels and compromised antioxidant defenses, making them more susceptible to the oxidative damage triggered by AIE-COF-mediated phototherapy. This difference in cellular responses underpins the selective cytotoxicity observed in cancer cells.

https://doi.org/10.1038/s41467-024-55430-4

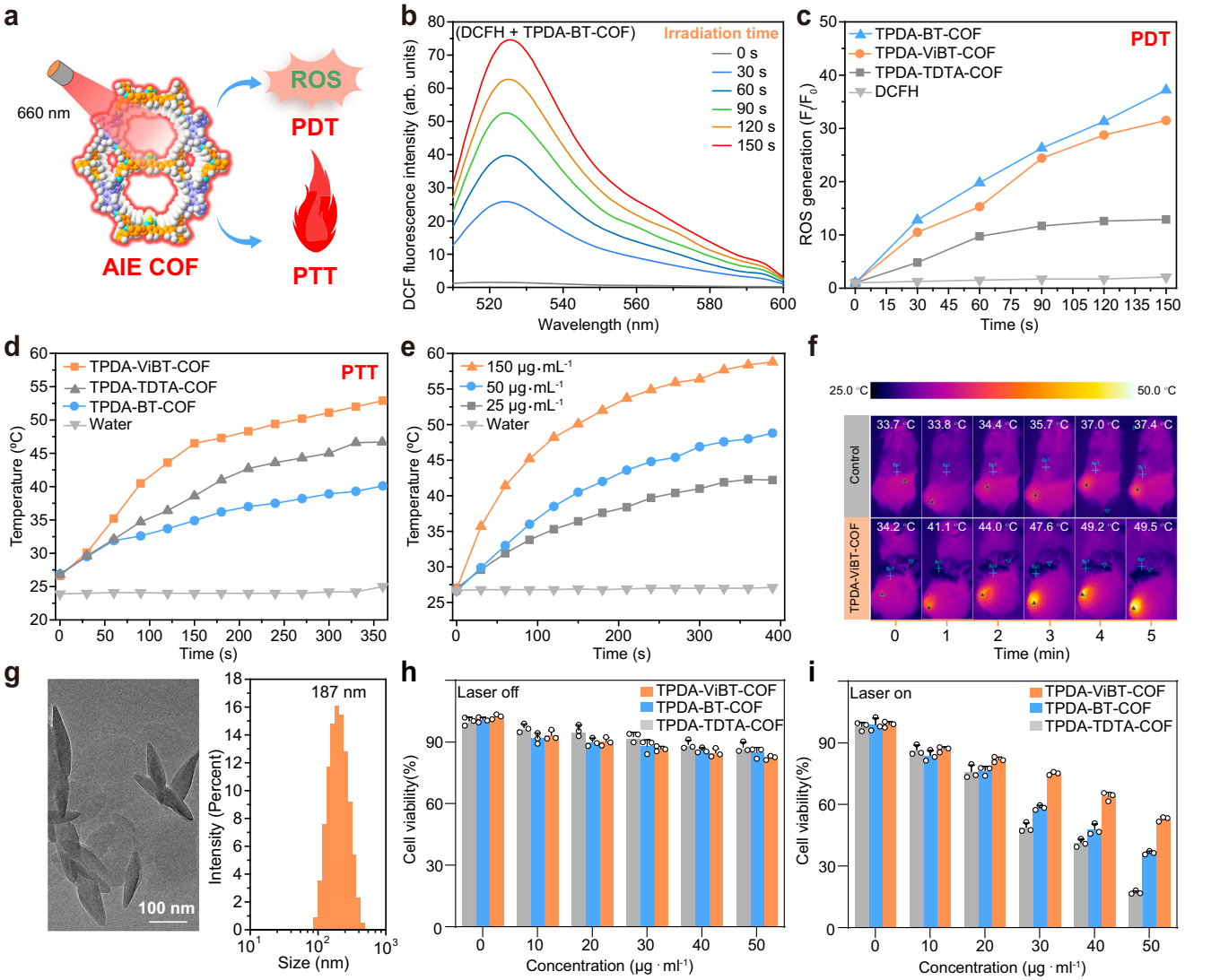

Fig. 4 | ROS generation and photothermal conversion capacity of TPDA-TDTA-COF, TPDA-BT-COF, and TPDA-ViBT-COF. a Illustration of the AIE COFs for efficient ROS generation and photothermal conversion. **b** ROS generation assessment of TPDA-BT-COF. **c** Comparison of the ROS production capacity of TPDA-TDTA-COF, TPDA-BT-COF, and TPDA-ViBT-COF. **d** Temperature change of TPDA-TDTA-COF, TPDA-BT-COF, and TPDA-ViBT-COF irradiated under a 660 nm laser irradiation with power density of 1.0 W cm^{-2}. **e** Temperature change of TPDA-ViBT-COF with different concentrations. **f** In vivo thermal images of mice with or without TPDA-ViBT-COF treatment. **g** TEM images and particle size distribution of TPDA-ViBT-COF. Data were repeated thrice independently with similar results. Cytotoxicity of TPDA-TDTA-COF, TPDA-BT-COF, and TPDA-ViBT-COF without (**h**) or upon 660 nm laser irradiation (**i**), n = 3 independent samples, data are presented as mean ± SEM. PDT photodynamic therapy, PTT photothermal therapy, DCFH 2,7-Dichlorodihydrofluorescein diacetate, ROS reactive oxygen species. Source data are provided as a Source Data file.

The therapeutic effect of AIE COFs in MC38 tumor-bearing mice

After assessing the photo cytotoxicity of these AIE COFs in vitro, the MC38-tumor-bearing mouse model widely employed in TLS-related research was established to in vivo investigate their anti-tumor performance (Fig. 5a)[57]. An effective inhibition of MC38 tumor growth was achieved by treatment with AIE COFs upon laser irradiation, while TPDA-ViBT-COF+laser treatment resulted in the near-complete eradication of tumors, demonstrating its outstanding therapeutic efficacy (Fig. 5b, c). Similar results were observed in the immunohistochemical staining images, where a substantial decrease in Ki-67 expression was observed in TPDA-ViBT-COF+laser-treated tumor tissues (Supplementary Fig. 15a, b). Also, an obvious increase in cleaved-caspase 3, Calreticulin, high mobility group protein B1, adenosine triphosphate, and expression was detected (Supplementary Fig. 16a, c). These results provide further support for the effective enhancement of immune response mediated by TPDA-ViBT-COF. Furthermore, no noticeable body weight loss or major organ damage was observed in mice after being subjected to different treatments, demonstrating the good biosafety of these AIE COFs (Fig. 5d and Supplementary Fig. 17).

To delve deeper into the influence of TPDA-ViBT-COF on the anti-tumor immune response, we analyzed the changes in immune cells in the tumor, tumor-draining lymph nodes (TDLN), and spleen (SP) on the 15 days after treatment (Supplementary Figs. 18–20). Results displayed that the TPDA-ViBT-COF+laser treatment was effective in activating the dendritic cells (DCs) in TDLN, which was essential for initiating the host immunity (Fig. 5l), and populating T cells in tumor, TDLN, and SP (Supplementary Fig. 21), possibly due to the effect of antigen presentation by the activated DC. Moreover, in the tumor, we also observed an increase in $CD3^+$ T and $CD4^+$ effector memory T cells, as well as a decrease in MDSCs within TPDA-ViBT-COF+laser treated tumor tissues (Fig. 5e–g). Additionally, an obvious increase in $CD4^+$ and $CD8^+$ antitumor central memory T cells was observed in TDLN and spleen (Fig. 5h, k), whereas the immunosuppressive myeloid-derived suppressor cells (MDSCs) were markedly decreased (Supplementary

https://doi.org/10.1038/s41467-024-55430-4

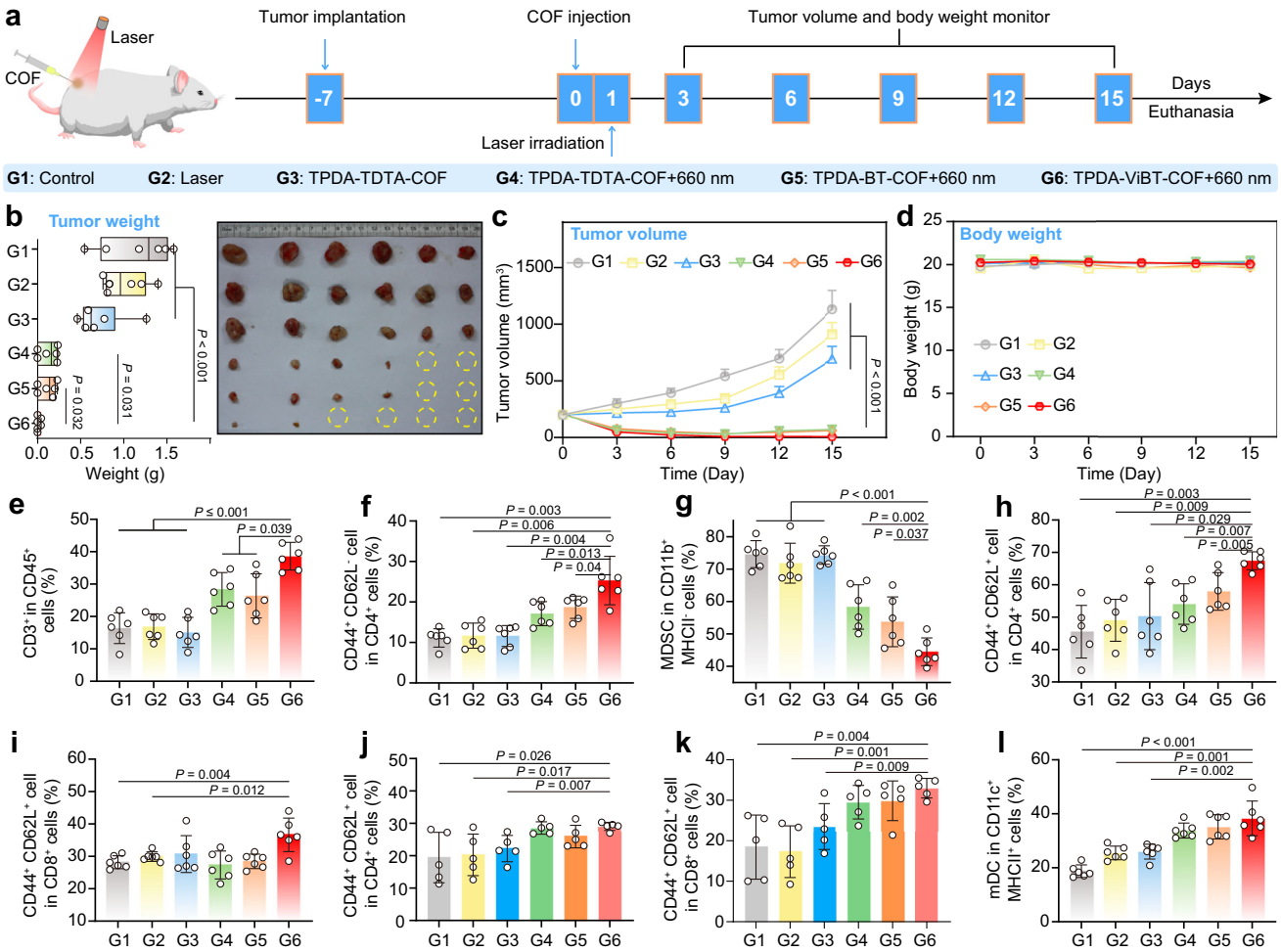

Fig. 5 | Antitumor effects of TPDA-TDTA-COF, TPDA-BT-COF, and TPDA-ViBT-COF in an MC38 tumor-bearing mice model. a The treatment protocol of AIE COF-mediated antitumor effects. **b** The images and the weight of MC38 tumors on day 15 and presented as box plots showing median with whiskers at minimum and maximum values, n = 6 independent samples. $P_{G(1\ vs\ 6)} = 0.0008$, $P_{G(2\ vs\ 6)} = 0.0001$, $P_{G(3\ vs\ 6)} = 0.0004$. **c** Tumor volume of MC38 tumor-bearing mice, n = 6 independent samples. $P_{G(1\ vs\ 6)} = 0.0003$, $P_{G(2\ vs\ 6)} = 0.0004$, $P_{G(3\ vs\ 6)} = 0.0007$. **d** Body weights of MC38 tumor-bearing mice, n = 6 independent samples. **e** Quantification of T cell ($CD3^+$) gating on $CD45^+$ cells in tumor, n = 6 independent samples. $P_{G(1\ vs\ 6)} = 0.0002$, $P_{G(2\ vs\ 6)} = 0.0004$, $P_{G(3\ vs\ 6)} = 0.0012$. **f** Quantification of $CD4^+$ T_{EM} ($CD44^+CD62L^-$) in tumor, *n* = 6 independent samples. **g** Quantification of MDSC gating on $CD11b^+$ $MHCII^-$ cells in tumor, n = 6 independent samples. $P_{G(1\ vs\ 6)} = 1.42E\text{-}05$, $P_{G(2\ vs\ 6)} = 5.72E\text{-}05$, $P_{G(3\ vs\ 6)} = 1.44E\text{-}05$. **h** Quantification of the gating of $CD4^+$ T_{CM} ($CD44^+CD62L^+$) on $CD3^+$ $CD4^+$ in both TDLN, n = 6 independent samples. $P_{G(1\ vs\ 6)} = 0.0002$, $P_{G(2\ vs\ 6)} = 0.0004$. **i** Quantification the gating of $CD8^+$ T_{CM} ($CD44^+CD62L^+$) on $CD3^+$ $CD8^+$ in TDLN, n = 6 independent samples. **j** Quantification the gating of $CD4^+$ T_{CM} ($CD44^+CD62L^+$) on $CD3^+$ $CD4^+$ in spleen, n = 5 independent samples. **k** Quantification the gating of $CD8^+$ T_{CM} ($CD44^+CD62L^+$) on $CD3^+$ $CD8^+$ in spleen, n = 5 independent samples. **l** Quantification of mDC in the TDLN, n = 6 independent samples. $P_{G(1\ vs\ 6)} = 9.19E\text{-}05$. Data are presented as mean ± SEM and statistical significance was assessed using one-way ANOVA with post hoc Tukey test was used when comparing more than two groups. Source data are provided as a Source Data file.

Fig. 21). These results altogether suggested that the TPDA-ViBT-COF-mediated phototherapy not only alleviated the immunosuppressive microenvironment but also activated the host defense system for effective immunotherapy, which may facilitate the development of iTLS in tumors (Fig. 6a).

TPDA-ViBT-COF-meditated phototherapy for inducing iTLS formation

To explore the potential of TPDA-ViBT-COF-mediated phototherapy in inducing the iTLS formation, we conducted multiplex immunohistochemistry to monitor the majority of iTLS-associated immune cells in tumor tissues treated or without treated with TPDA-ViBT-COF+laser. Intriguingly, we observed extensive leukocyte aggregates including an inner B cell zone surrounded by dispersed $CD4^+$T cells in TPDA-ViBT-COF treated tumors, indicating the potential formation of iTLS in tumor tissues (Fig. 6b, Supplementary Figs. 21 to 23 and Supplementary Fig. 34). To further confirmed the occurrence of iTLS formation in TPDA-ViBT-COF+laser treated tumors, scRNA-seq analysis was employed[58,59]. After quality control, a total of 17182 cells were segregated into 9 distinct cell populations, including epithelial cells, stromal cells, macrophages, plasma cells, NK cells, $CD4^+$ T cells, B cells, Treg cells, and $CD8^+$ T cells, based on the graph-based clustering using canonical marker genes' average expression (Fig. 6c, d and Supplementary Fig. 23 to 25).

Non-immune cell subsets such as epithelial and stromal cells are primarily composed of tumor cells and tumor-related fibroblasts. In this work, a sharp reduction in the proportion of epithelial (tumor) and stromal cells and a notable increase in B cells and $CD4^+$ T cells was observed after treatment with TPDA-ViBT-COF (Fig. 6d, e). This may be attributed to the cytotoxic effect of TPDA-ViBT-COF-mediated phototherapy reducing the proportion of tumor cells. Additionally, the release of tumor antigens and inflammatory cytokines increases the infiltration of immune effector cells. The reduction in the tumor and stromal cell ratio, combined with the increase in immune cell

https://doi.org/10.1038/s41467-024-55430-4

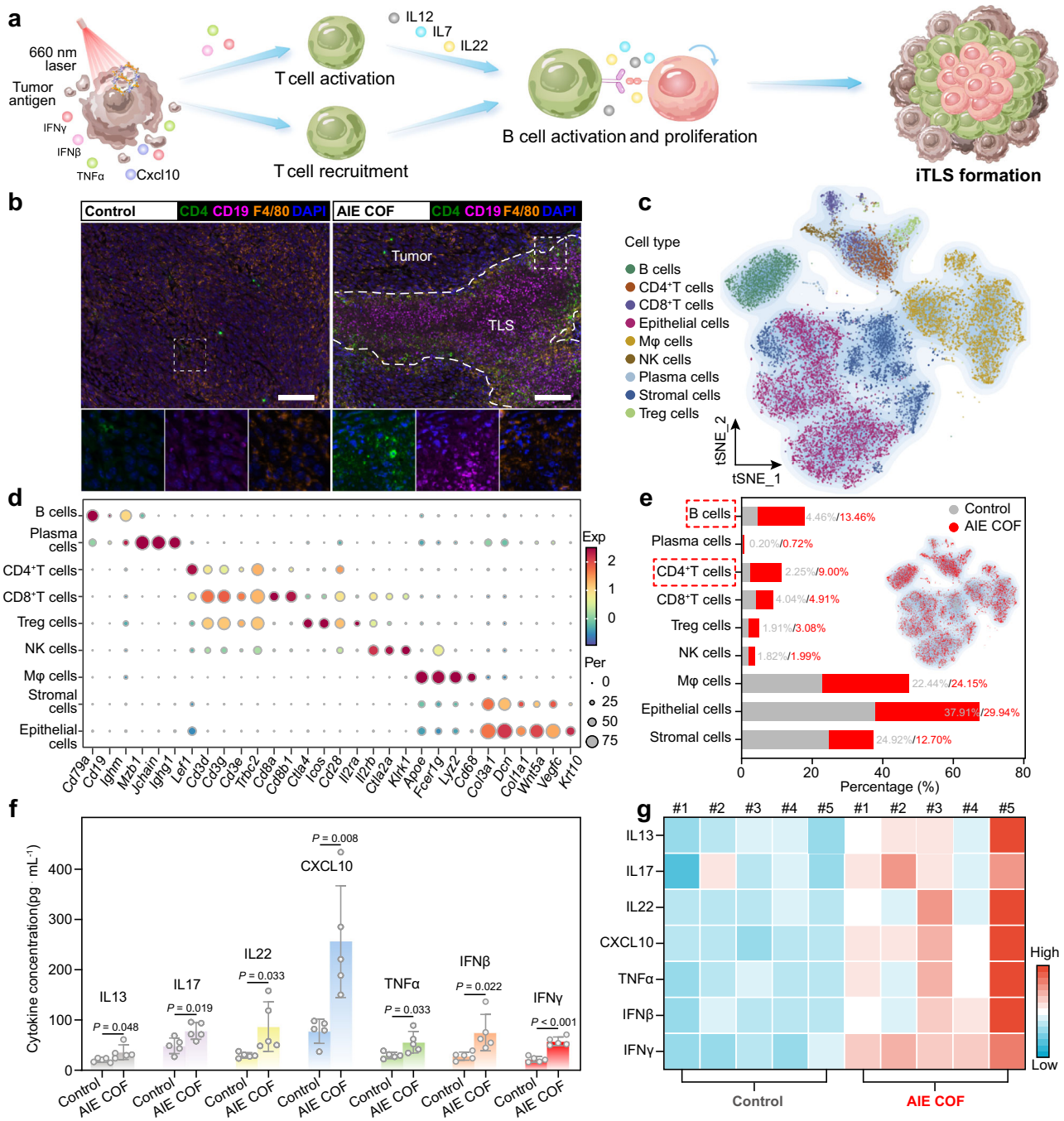

Fig. 6 | TPDA-ViBT-COF-meditated phototherapy for inducing TLS formation. **a** Schematic illustration of the occurrence of TLS formation triggered by TPDA-ViBT-COF-meditated phototherapy. **b** Representative images of mIHC staining of CD4 (green), CD19 (magenta), F4/80 (yellow), and DAPI (blue) in MC38 tumor after and before TPDA-ViBT-COF treatment, scale bar: 50 μm. Data were repeated 4 times independently with similar results. **c** t-Distributed stochastic neighbor embedding plots of 17182 cells from MC38 tumor treatment with TPDA-ViBT-COF-meditated phototherapy. **d** A dot plot was generated to display the highly expressed marker genes in each major cell type. **e** A stacked histogram was employed to depict the percentages of different cell types among total cells, with or without TPDA-ViBT-COF treatment. **f** Quantification of the levels of various cytokines and chemokines in tumors following treatment with control or TPDA-ViBT-COF, n = 5 independent samples, data are presented as mean ± SEM and statistical significance was assessed using two-tailed Student's t-test, $P_{G(IFNγ)} = 0.0003$. **g** A heat map was generated to visualize the distribution of IL13, IL17, IL22, CXCL10, TNFα, IFNβ, and IFNγ levels within each tumor, n = 5 independent samples. Source data are provided as a Source Data file.

proportion, collectively led to a decrease in the proportion of non-immune cells.

iTLS formation is driven by the excessive accumulation of pro-inflammatory cytokines in tumor tissues, which regulate the maturation, proliferation, and migration of B cells and T cells in the DLN[60,61]. To elucidate the potential mechanism underlying TPDA-ViBT-COF-mediated phototherapy in inducing the formation of iTLS, we employed an ELISA kit to assess the secretion of pro-inflammatory cytokines. By co-culturing primary DCs with TPDA-ViBT-COF-treated MC38 tumor cells, we observed an obvious elevation in the levels of Cd80 and Cd86 signals in the AIE COF treatment group, indicative of DC maturation. Additionally, the concentration of CCL19 and CCL21 in the supernatants of DCs displayed a notable increase, suggesting that TPDA-ViBT-COF can initiate iTLS formation by promoting the

https://doi.org/10.1038/s41467-024-55430-4

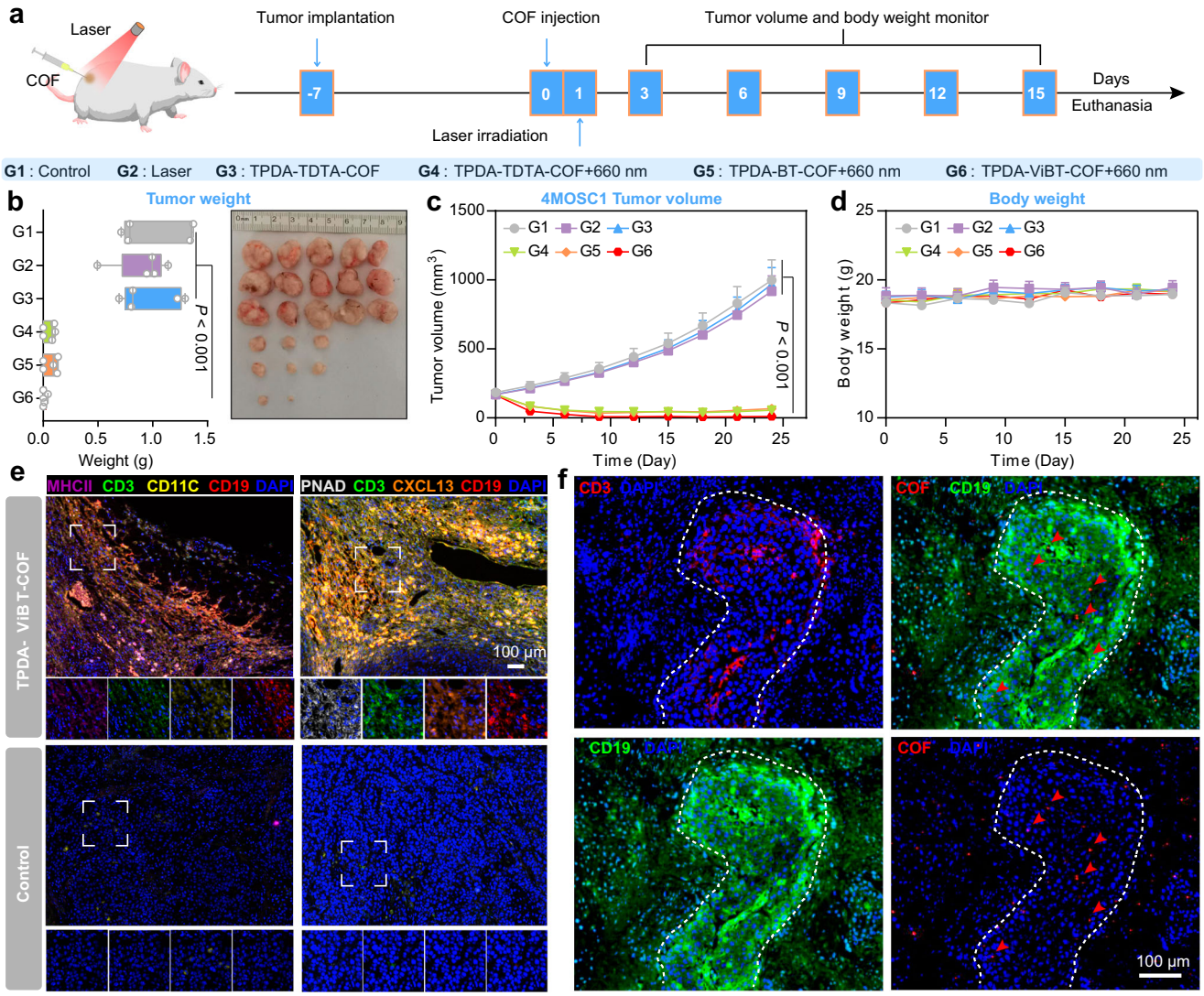

Fig. 7 | TPDA-ViBT-COF-meditated phototherapy for inducing iTLS formation in 4MOSC1-tumor bearing mice. a The treatment protocol of AIE COF-mediated antitumor effects. **b** The images and the weight of 4MOSC1 tumors on day 15, and presented as box plots showing median with whiskers at the minimum and maximum values, $n = 5$ independent samples, $P_{G(1\ vs\ 6)} = 0.0010$, $P_{G(2\ vs\ 6)} = 0.0007$, $P_{G(3\ vs\ 6)} = 0.0005$. Tumor volume (**c**) and body weight (**d**) of 4MOSC1 tumor-bearing mice, n = 5 independent samples, $P_{G(1\ vs\ 6)} = 0.0010$, $P_{G(2\ vs\ 6)} = 0.0007$, $P_{G(3\ vs\ 6)} = 0.0005$. **e** Representative images of mIHC staining of CD19 (red), CD3 (green), PNAD (white), CD11C (yellow), MHCII (magenta), CXCL13 (orange), and DAPI (blue) in 4MOSC1 tumor with or without TPDA-ViBT-COF treatment. Data were repeated thrice independently with similar results. **f** Representative fluorescence images of 4MOSC1 tumor sections after and before TPDA-ViBT-COF treatment. Data were repeated thrice independently with similar results. Data are presented as mean ± SEM and statistical significance was assessed using one-way ANOVA with post hoc Tukey test was used when comparing more than two groups. Source data are provided as a Source Data file.

secretion of CCL19 and CCL21 (Supplementary Fig. 26). We also investigated the effects of AIE COF-treated MC38 cells on macrophages. The results showed an increase in CD86 expression and a decrease in CD206 expression in RAW264.7 cells, indicating that AIE COF-treated MC38 cells can promote M1 macrophage polarization (Supplementary Fig. 27). Moreover, TPDA-ViBT-COF-mediated phototherapy effectively augmented the secretion of specific cytokines, including CXCL10, TNFα, IFNγ, and IFNβ, within the tumor tissue. This enhanced cytokine secretion favored the localization and maturation of T lymphocytes within the tumor microenvironment (Fig. 6f, g). Furthermore, another set of cytokines (IL22, IL7, and IL13) that boost the maturation and proliferation of B cells was also overexpressed upon post-treatment with TPDA-ViBT-COF+laser (Fig. 6f, g). Taken together, these findings collectively unveil the capacity of TPDA-ViBT-COF mediated phototherapy to effectively induce the formation of iTLS through promoting cytokine hypersecretion to facilitate the T and B cell maturation, proliferation, and migration.

TPDA-ViBT-COF-meditated phototherapy for inducing iTLS formation in 4MOSC1-tumor-bearing mice

In order to further validate the capacity of TPDA-ViBT-COF in inducing iTLS formation, we performed additional in vivo experiments utilizing the 4NQO-induced murine oral squamous cells (4MOSC1) tumor-bearing mouse model. This specific mouse model is widely recognized for its notable immune cell infiltration, rendering it an optimal selection to explore the efficacy of TPDA-ViBT-COF in fostering iTLS formation[62–64]. Following the establishment of tumor models, mice bearing 4MOSC1 tumors were randomly assigned to six treatment groups: PBS, Laser, TPTA-TDTA-COF, TPTA-TDTA-COF+laser, TPDA-BT-COF+laser, and TPDA-ViBT-COF+laser (Fig. 7a). On day 24 post-treatment, the mice were euthanized, and tumor samples were

collected and weighed. Notably, the treatment with TPDA-ViBT-COF resulted in a grave inhibition of tumor growth, leading to the elimination of approximately 80% of tumors (Fig. 7b–c). Moreover, no apparent weight loss was observed among the different treatment groups, indicating the favorable biocompatibility of TPDA-ViBT-COF (Fig. 7d). Subsequently, we performed mIHC to detect iTLS-associated cells in 4MOSC1 tumor tissues treated with or without TPDA-ViBT-COF +laser. Similar to the previous results in MC38 tumor tissue, we observed areas of T cell and B cell aggregation, where scattered dendritic cells were also visible, further proving the formation of iTLS (Fig. 7d). Additionally, we detected the expression of PNAD-positive high endothelial venules cells and CXCL13 within the iTLS, suggesting that TPDA-ViBT-COF facilitates the recruitment of immune cells to the tumor site by promoting angiogenesis and secreting CXCL13, thus contributing to iTLS formation (Fig. 7e and Supplementary Figs. 28 to 33). Furthermore, intense red fluorescence originating from TPDA-ViBT-COF was observed specifically within regions corresponding to iTLS, confirming the role of TPDA-ViBT-COF in eliciting iTLS formation (Fig. 7f). Additionally, we used immunohistochemistry to calculate the area of B cell aggregation in the tumor tissue and preliminarily estimated the volume percentage of AIE COF-induced iTLS based on tumor volume data. We found that in the MC38 tumor tissues treated with AIE COF, the number of TLS was approximately 1-2, accounting for an average of 0.195% of the total tumor volume. In the 4MOSC1 tumor tissues, the number of TLS was ~1–3, accounting for 0.574% of the total tumor volume (Supplementary Fig. 33). Taken together, these results provide robust evidence supporting the remarkable ability of TPDA-ViBT-COF to induce iTLS. Given that iTLS formation has been shown to enhance leukocyte recruitment to the tumor microenvironment and improve the efficacy of immunotherapy, we propose that TPDA-ViBT-COF-mediated iTLS formation may synergistically enhance the immunotherapy effects[9].

TPDA-ViBT-COF-mediated ICB

Immune checkpoint blockade therapy, which blocks PD-1 or CTLA-4, has generated significant interest due to its ability to induce specific anti-tumor immune responses. Although PD-1 is generally considered the most effective ICB inhibitor for achieving desirable therapeutic efficacy, the relative efficacy of different ICB inhibitors has not been extensively studied. Herein, we try to utilize scRNA-seq to investigate an appropriate immune checkpoint when combined with TPDA-ViBT-COF-mediated phototherapy. The results indicated that CTLA-4 blockade may be a better partner than PD-1 blockade when combined with TPDA-ViBT-COF-mediated phototherapy. Specifically, the T cells were re-clustered and 7 sub-clusters were identified, including naive $CD4^+$ and $CD8^+$ T cells (T_N), $CD4^+$ central memory T cells (T_{CM}), $CD8^+$ effector exhausted and effector memory T cells (T_{EX} and T_{EM}), regulatory T cells (T_{REG}), and follicular T regulatory cells (T_{FR}) (Fig. 8a). The functional signatures of these T cell subsets were then annotated using the expression of known signature genes (Fig. 8c). The $CD8^+$ T_{EX} are recognized to exhibit elevated expression of *Pdcd1*, *Lag3*, and *Havcr2*, which serve as markers for the efficacy of conventional αPD-1 immunotherapy. However, the fraction of $CD8^+$ T_{EX} sharply decreased from 34.18% to 6.39% after TPDA-ViBT-COF+laser treatment. In contrast, the abundance of T cell subsets ($CD4^+$ and $CD8^+$ T_N, $CD8^+$ T_{EM}, and $CD4^+$ T_{CM}) that exhibited lower expression of *Pdcd1*, *Lag3*, and *Havcr2* were drastically increased in tumors treated with TPDA-ViBT-COF+laser. On the other hand, the M1 macrophages are known to possess robust neoplastic cell phagocytic and antigen-presenting capability, thus, they show effective activation of the immune system and improved immunotherapy outcomes than M2 macrophages[65,66]. In this study, the impact of TPDA-ViBT-COF on macrophage polarization towards the M1 or M2 state was examined by categorizing the macrophages into four subtypes ($Atf2^+$Mφ, $C1qc^+$Mφ, $Isg15^-$Mφ, and $Ly6c2^+$Mφ) and evaluating their polarization scores across these macrophage subpopulations (Fig. 8d, f). As displayed in Fig. 8f, a notable tendency towards an M1-like transcriptional program was observed within the $Ly6c2^+$Mφ subtype, whereas the $C1qc^+$Mφ subtype exhibited a transcriptome indicative of a more M2-related phenotype. Notably, the tumors subjected to TPDA-ViBT-COF treatment demonstrated a 1.69-fold rise in the M1 phenotype of $Ly6c2^+$Mφ cells (Fig. 8e), suggesting that the TPDA-ViBT-COF-mediated phototherapy could confer benefits in immune system activation and augment the effectiveness of immunotherapy. To further investigate the cell chat that specifically occurs in TPDA-ViBT-COF treated tumors, we performed the CellphoneDB algorithm to calculate the ligand-receptor interactions among the major cell population (Fig. 8g). Among these immune cell, macrophage and plasma cells exhibited increased ligand-receptor paired with tumor cells in the condition of TPDA-ViBT-COF treatment, implying these cell lineages may reprogram by TPDA-ViBT-COF treaded tumor cells (Fig. 8i). As demonstrated in Fig. 8h, the Ctla4-Cd86 interaction pair was more prevalent in TPDA-ViBT-COF+laser treated tumors than in the control group, suggesting that the Ctla4-Cd86 axis may contribute to the immune evasion. Although the increased expression of *Ctla4* was not detected in Treg cells, obvious enhanced expression of its associated ligand Cd86 was noted in both B cells and Mφ cells (Fig. 8j). Furthermore, the mIHC analysis also confirmed the increased expression of Cd86 in B cells and macrophages and suggested that the overstimulation of the Ctla4-Cd86 axis was primarily attributed to the upregulation of *Cd86* (Fig. 8k and Supplementary Fig. 35). As PD-1 blockade is also relevant in setting of myeloid cell PD-L1 expression, we also assessed PD-L1 expression on the surface of tumor cells following TPDA-ViBT-COF combined with laser treatment. Flow cytometry analysis showed no obvious increase in PD-L1 expression on $CD45^-$ cells in tumor tissues treated with TPDA-ViBT-COF+Laser compared to the control group. The PD-L1 immunofluorescence staining experiment of tumor tissues also verified the above conclusion (Supplementary Fig. 35). Collectively, these results indicated that the inhibition of the interaction between Ctla4 and Cd86 might confer better therapeutic benefits when used in combination with TPDA-ViBT-COF.

Synergistic effect of TPDA-ViBT-COF + αCTLA4

Based on the impressive in vivo results and scRNA-seq analysis, we hypothesized that the TPDA-ViBT-COF-mediated phototherapy in combination with CTLA-4 blockade may maximize the treatment efficacy. To validate this hypothesis, we established a dual-flank mice model bearing MC38 tumors and investigated the synergistic effect of TPDA-ViBT-COF with αCTLA-4 (Fig. 9a). As a positive control group, we also evaluated the synergistic effect of TPDA-ViBT-COF with αPD-1. As shown in Fig. 9b, c, the combination of TPDA-ViBT-COF+laser with αCTLA-4 exhibited the lowest tumor volume in both primary and distant tumors. This was further confirmed by the bioluminescence imaging at different time points (Fig. 9e). Furthermore, the survival time of mice in the TPDA-ViBT-COF+laser+αCTLA-4 group was effectively prolonged, and all mice survived at day 60, in contrast almost all mice in other groups reached the endpoints (Fig. 9d). To investigate the immune memory effect of TPDA-ViBT-COF+laser combined with αCTLA-4, we also established an MC38 rechallenged mice model (Fig. 9f), where the mice treated with TPDA-ViBT-COF+laser+αCTLA-4 showed no detectable tumor recurrence (Fig. 9g, h), whereas the untreated mice suffered from grave tumor recurrence. These results indicate that the TPDA-ViBT-COF+laser+αCTLA-4 represents a promising approach for establishing a durable and robust immune memory protection system, effectively suppressing tumor growth and preventing recurrence.

Discussion

Promoting the iTLS formation within tumor tissues has been identified as a promising avenue for enhancing the efficacy of cancer

https://doi.org/10.1038/s41467-024-55430-4

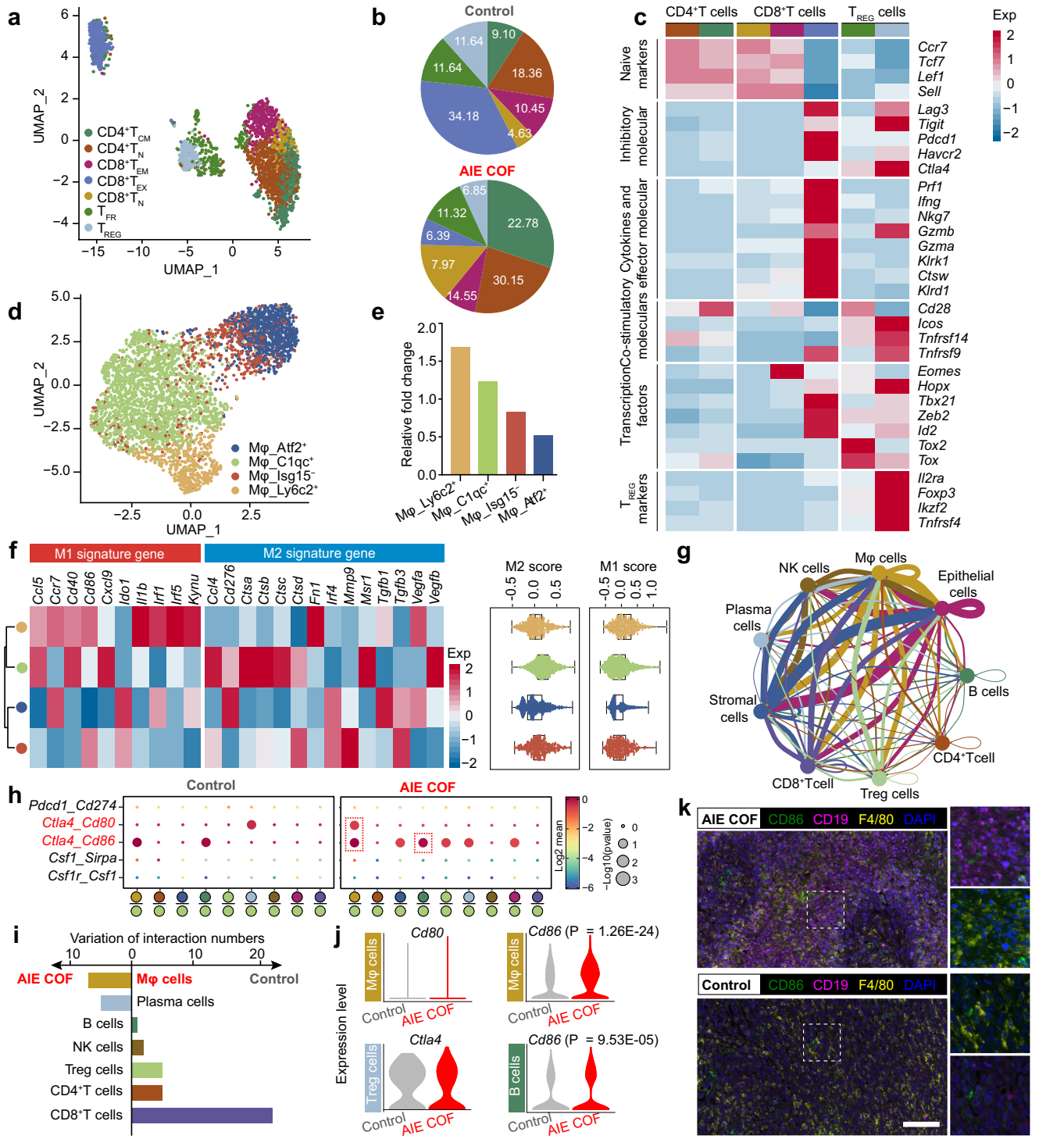

Fig. 8 | scRNA-seq was used to dissect the potential immunotherapy targets for TPDA-ViBT-COF-mediated phototherapy in MC38-tumor-bearing mice. **a** Visualization of the T cell subsets using Uniform manifold approximation and projection (UMAP). **b** A pie chart was generated to display the percentages of distinct cell subtypes among T cells treatment with control or AIE COF. The z-score normalized mean expression levels of T cell function-associated genes. **c** In each cell cluster, as well as M1 and M2 signature genes (**f**) in each Mφ cell cluster and presented as box plots showing median with whiskers at minimum and maximum values, n = 3988 biologically independent cells. **d** UMAP visualization of Mφ cell subsets. **e** Histogram chart showing the relative fold change of Mφ cell subsets under different treatments. **g** Overview of chosen ligand-receptor interactions among various cell types. **h** A bubble plot was employed in this study to illustrate changes in selected ligand-receptor interactions with or without TPDA-ViBT-COF treatment, statistical significance was calculated using a permutation test, assessing the significance of cell-cell communication by comparing observed mean expression with a null distribution generated by random permutations. **i** The variation of ligand-receptor pair between immune cell subtypes and epithelial cells with or without TPDA-ViBT-COF treatment. **j** A violin plot was utilized to depict the expression levels of specific genes in B cells, Mφ cells, and Treg cells. The p-values were computed using a two-tailed Student's t-test. **k** Representative multiplexed immunohistochemical staining images of CD19 (magenta), CD86 (green), F4/80 (yellow), and DAPI (blue) in MC38 tumor samples that underwent treatment with either control or AIE COF, scale bar: 50 μm. Data were repeated 4 times independently with similar results. scRNAseq data are available through the Gene Expression Omnibus with accession number GSE268619.

https://doi.org/10.1038/s41467-024-55430-4

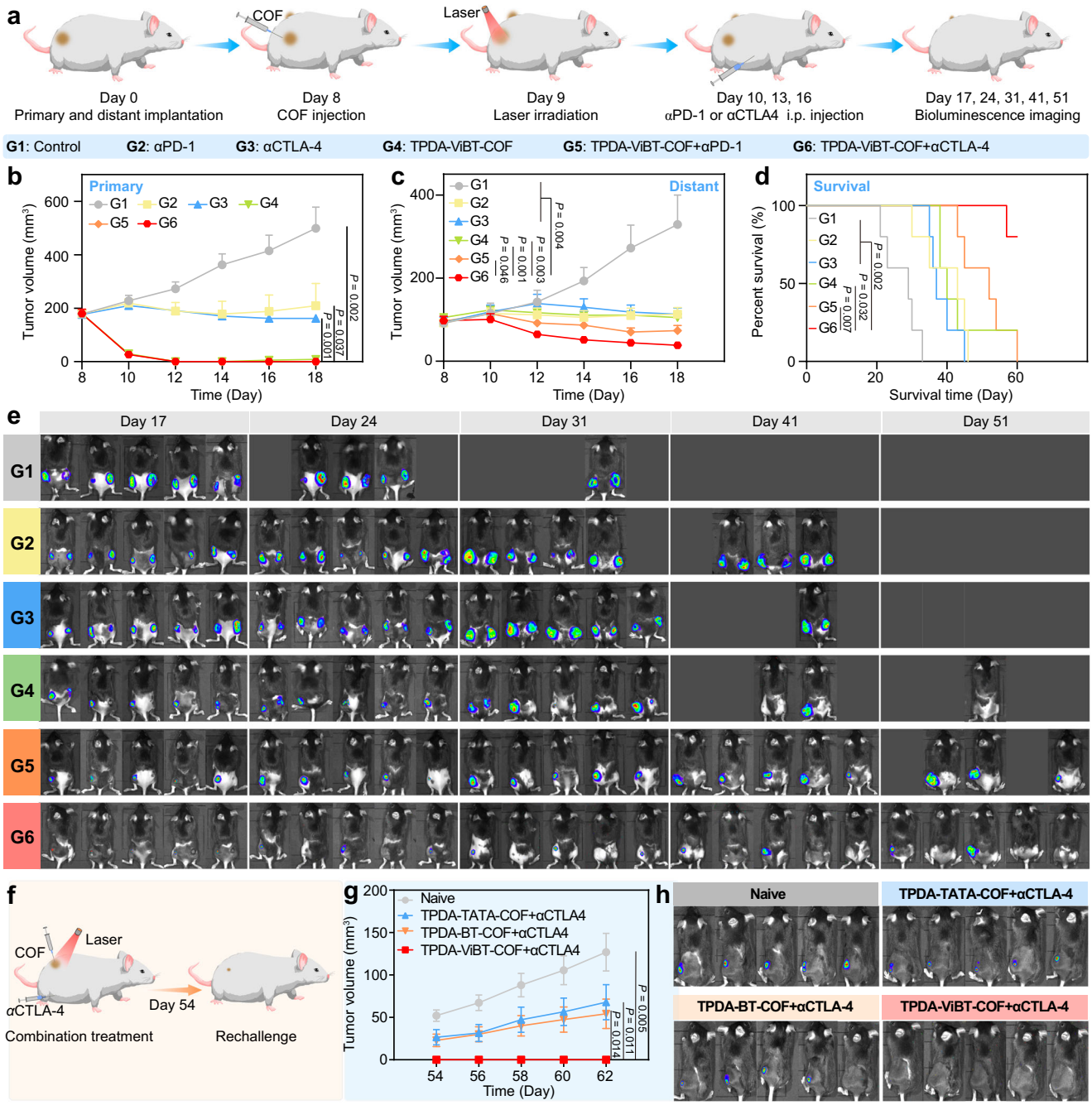

Fig. 9 | TPDA-ViBT-COF-mediated ICB. a Schematic illustration of the combination therapy of TPDA-ViBT-COF + αCTLA4. The tumor growth curves of primary (**b**) and distant (**c**) and the percentage of survival (**d**) among MC38 mice following various treatments, n = 5 independent samples. **e** Bioimages of MC38 mice following various treatments. **f** The treatment protocol of rechallenge experiments. **g** The growth curve of tumors in the control, TPDA-TDTA-COF + αCTLA4, TPDA-BT-COF + αCTLA4, and TPDA-ViBT-COF + αCTLA4, n = 6 independent samples. **h** Bioluminescence images of mice in the naïve, TPDA-TDTA-COF + αCTLA4, TPDA-BT-COF + αCTLA4, and TPDA-ViBT-COF + αCTLA4, n = 5 independent samples. Data in this study are presented as mean ± SEM and statistical significance was determined by performing one-way ANOVA with the post hoc Tukey test used when comparing more than two groups. Survival analysis was conducted using the log-rank Mantel-Cox test. Source data are provided as a Source Dat a file.

immunotherapy[7–9]. These ectopic lymphoid organs present a unique opportunity to augment immune responses by facilitating lymphocyte infiltration and optimizing antigen presentation. Despite their potential, the current lack of effective methodologies to elicit the iTLS formation represents a substantial hurdle, underscoring the pressing need to develop innovative strategies in this field. Herein, a series of AIE COFs were designed and investigated for promoting the formation of iTLS and enhancing antitumor immunity. Detailed mechanistic inquiry unveiled that the phototherapeutic efficacy of these AIE COFs could be drastically amplified through a synergistic approach employing electron-acceptor and π-bridge engineering strategies. Previous studies have demonstrated that tumor cells release inflammatory cytokines such as TNFα, IFNγ, and CXCL10 under stress conditions[67–69]. In this study, we found that AIE COF-mediated phototherapy effectively promotes the release of these inflammatory factors by inducing thermal and chemical damage directly to the tumor cells.

These dying tumor cells can then act as an in situ vaccine, activating DCs. Subsequently, mature DCs secrete cytokines such as CCL19 and CCL21, to facilitate the recruitment of T cells and B cells into the tumor, allowing the formation of T cell zones and B cell zones within the TLS[70,71]. Furthermore, the inflammatory cytokines secreted by tumor cells, including CXCL10, TNFα, IFNγ, and IFNβ, promote the localization and maturation of T lymphocytes within the TME[67]. We also confirmed increased intratumoral T-cell infiltration using scRNA-seq and flow cytometry analysis. Our scRNA-seq data validated that this increase in T cell content was accompanied by elevated levels of T cell-associated cytokines, such as IL22, IL7, and IL13, which are essential for B cell maturation and proliferation[72–74]. In addition, the mIHC results also unveiled that mature dendritic cells and dying tumor cells, along with inflammatory cytokines, facilitate the recruitment and proliferation of B cells and T cells, ultimately forming B cell and T cell clusters within the TLS.

Although various nanomedicines have been developed to sensitize tumors to ICB therapy, few studies have identified the optimal immune combination targets for specific nanomedicines. In this study, we observed that the proportion of CD8 T_{EX} cells expressing high levels of PD-1, LAG3, and HAVCR2 decreased in tumor tissues following AIE COF treatment. Additionally, flow cytometry and immunofluorescence analyses indicated that PD-L1 expression in tumor tissues did not increase post-treatment with AIE COF. Our scRNA-seq results, corroborated by mIHC findings, identified CTLA4-CD86 as the primary immune inhibitory pathway in tumors treated with AIE COF. Notably, in vivo, experiments demonstrated that combining AIE COF with CTLA4 blockade yielded stronger antitumor effects and drastically extended the survival of mice with bilateral tumors, compared to PD-1 blockade. This suggests that CTLA4 blockade may be more effective than PD-1 blockade when used in conjunction with AIE COF.

However, this study has limitations. While scRNA-seq provides valuable insights into the transcriptomic state at the single-cell level, its limited reading depth might omit genes that reflect tumor cell vulnerability, which could inform the improved design of AIE COF. Moreover, although we confirmed that AIE COF-mediated phototherapy induces the formation of iTLS, it is crucial to elucidate the dynamic changes in cellular composition within iTLS at different maturation stages to fully understand their development and functionality. Besides, the 660 nm laser used in this study has limited penetration depth. For superficial tumors, intratumoral injection is an effective administration strategy, ensuring that the treatment is localized directly within the tumor, thereby maximizing efficacy while minimizing systemic exposure and potential side effects. For deeper tumors, we propose that intravenous injection of COF nanomedicines with near-infrared-II window absorption, coupled with the subcutaneous implantation of wearable laser devices, could enhance the feasibility of translating this technology into clinical applications. Additionally, our method showed limited efficacy in cold tumors, where immune cells are not naturally present within the tumor microenvironment, making TLS induction more challenging. This limitation suggests that combining AIE COF therapy with other immune-modulating strategies, such as Chimeric Antigen Receptor T-cell immunotherapy, may be necessary to trigger TLS formation in such contexts. This research represents a COF-based iTLS inducer to potentiate cancer immunotherapy, highlighting the promising potential of COF materials in biomedical applications.

Methods

Ethical Statements

Ethical approval for this study was obtained from the Animal Ethics Committee of the School and Hospital of Stomatology, Wuhan University (approval number: S07920080I). All animal procedures complied with the Regulations for the Administration of Affairs Concerning Experimental Animals by the State Council of the People's Republic of China. Mice were maintained under specific pathogen-free (SPF) conditions, with a 12-h light/dark cycle, at ~22 °C and 50% humidity.

Cell culture and animal model

The MC38 (CBP60825) cells, MC38-luc (CBP30169L) cells, human oral keratinocyte (HOK) cells, mouse fibroblast cell line of L929 (CCL-1), mouse mononuclear macrophage RAW264.7 (TIB-71) cells and primary DCs were cultured in high glucose DMEM medium (1% penicillin/streptomycin and 10% FBS) under standard cell culture conditions at 5% CO_2 and 37 °C. The MC38, MC38-Luc, L929, and RAW264.7 cells were obtained from the American Type Culture Collection. The human oral keratinocyte (HOK) cell line was gifted by Shanghai Ninth People's Hospital, Shanghai Jiao Tong University. The MC38-luc cells were maintained similarly, with the addition of puromycin (1 μg mL^{-1}) to the medium. The murine squamous carcinoma cell line 4MOSC1 is gifted from Prof. J. Silvio Gutkind of the University of California San Diego via a material transfer agreement (SD2017-202). The 4MOSC1 cells were cultured in Keratinocyte serum-free medium (K-SFM, Gibco) culture conditions at 5% CO_2 and 37 °C. Female C57BL/6, aged 6–8 weeks and weighing 18–20 g, were obtained from the Hubei Provincial Academy of Preventive Medicine. After the treatment, the mice were euthanized, and the tumors were dissected for further analysis. All mice in this study were euthanized under CO_2 anesthesia if the volume of the primary tumor reached a maximum allowable volume of 2000 mm^3 or if the tumor burden compromised the animal welfare. The maximal tumor size in this study was not exceeded.

Cell viability

After treating the MC38, HOK, L929, and RAW264.7 cells with AIE COFs for 24 h, we replaced the medium and exposed the cells to 660 nm laser irradiation. The CCK8 was used to assess the cell viability post a 4-h incubation period.

Construction of TPDA-TDTA-COF, TPDA-BT-COF and TPDA-ViBT-COF

We synthesized the AIE COFs by placing M-TPDA (26.5 mg, 0.06 mmol) and an equal amount of either M-TDTA, M-BT, or M-ViBT, into a Pyrex tube, and then mesitylene (1.5 mL), dimethylacetamide (1.5 mL) and aqueous acetic acid (0.3 mL, 6 M) were added. After sealing and heating the tube at 120 °C for 72 h, the COF sample was centrifuged and washed with chloroform/acetone mixture solvent and then dried at 100 °C for 12 h.

Cell viability

Inoculate 3×10^4 MC38, HOK, L929, and RAW264.7 cells into each well of a 24-well plate. Once all cells have fully adhered to the plate, replace the original medium with a complete culture medium containing 30 μg mL^{-1} TCN-PPDA-COF. Incubate for 24 h and then replace with fresh culture medium. Subject cells to 660 nm laser (1.0 Wcm^{-2}, 5 min) irradiation. After a 4 h incubation period, assess the viability of cells using the CCK8 kit.

Immunofluorescence

Inoculate 3×10^4 MC38 cells into each well of a 24-well plate. Once all cells have fully adhered to the plate, replace the original medium with a complete culture medium containing AIE COFs (50 μg mL^{-1}). Incubate for 24 h and then replace with fresh culture medium. Subject MC38 cells to 660 nm laser (1.0 W cm^{-2}, 5 min) irradiation, fixed, rinsed, and permeabilized. Primary DCs co-cultured with MC38 cells likewise underwent fixed, rinsed, and permeabilized. After overnight incubation with primary antibodies (anti-HMGB1, anti-CD80, anti-CD86 antibodies, anti-LAMP1, anti-HSP60, and anti-GRP94 antibodies), the cells were subjected to a 1-h incubation period with a secondary antibody

conjugated to DyLight 488. The fluorescence intensity was determined via a confocal laser scanning microscopy after DAPI staining of the cell nucleus.

In vivo antitumor effects and flow cytometry

The antitumor efficacy of AIE COFs was evaluated using the MC38-tumor-bearing mouse animal model. To establish an MC38-tumor-bearing mouse animal model, a total of 1×10^6 MC38 cells was inoculated into the right blank of C57BL/6 mice. Following an eight-day post-injection period, the mice were randomly distributed among six groups with varying treatments (Control, 660 nm laser (1.0 W cm^{-2}, 5 min), TPDA-TDTA-COF, TPDA-TDTA-COF + 660 nm (1.0 W cm^{-2}, 5 min), TPDA-BT-COF + 660 nm (1.0 W cm^{-2}, 5 min), and TPDA-ViBT-COF + 660 nm laser (1.0 W cm^{-2}, 5 min)). AIE COFs in a dose of 5 mg kg^{-1} were administered to each group (intratumoral injection), and body weights and tumor volumes were monitored every three days. Upon euthanasia, the tumor weights and tumor photographs were recorded. Similarly, another group of MC38-tumor-bearing mouse animal models followed the above treatment strategy. After euthanasia, the lymph nodes and spleen were transformed into single-cell suspensions, stained with antibodies specific to the cells of interest, and analyzed using FACS caliber flow cytometer (Beckman) and FlowJo software (Tree Star).

Immunohistochemistry and multiplex immunohistochemistry

Immunohistochemistry was performed following standard protocols (antigen was retrieved using microwave treatment in either EDTA or citrate after a 100%, 95%, 90%, 80%, and 70% alcohol sequence. Goat serum was employed to avoid any non-specific binding of antibodies). All sections were scanned using the panoramic DESK digital pathology scanner (3D HISTECH). The Opal kit (PerkinElmer) was used for multiplex immunohistochemistry following the manufacturer's instructions. The relative expression of different immune biomarkers across samples was analyzed using the Vectra Polaris system (PerkinElmer).

Cytokine detection

Fresh tumor tissue samples were collected from mice before and after COF-mediated phototherapy treatment. The cytokine levels were measured using Mouse TNFα and IFNγ ELISA Kit (Servicebio), Mouse IL13, IL17, IL22, CXCL10, and IFN-β ELISA Kit (MULTI SCIENCES). For cell supernatant, the cytokine levels were measured using mouse CCL19 and CCL21 ELISA Kit (RUIXIN BIOTECH).

Abscopal effect

To evaluate the abscopal effect of TPDA-ViBT-COF, an MC38 tumor-bearing dual-flank model was established using CTLA4 and PD-1 as immune checkpoint inhibitors. The MC38 tumor-bearing dual-flank model was established in C57BL/6 mice by injecting 5×10^5 and 1×10^6 MC38-Luc cells in the left and right flank, respectively. On day 8, the mice were randomly distributed among six groups with varying treatments (Control, αCTLA-4, αPD-1, TPDA-ViBT-COF+laser, TPDA-ViBT-COF+laser+αPD-1, and TPDA-ViBT-COF+laser+αCTLA-4 groups). On days 10, 13, and 16, αPD-1 or αCTLA-4 was administered at a dose of 5 mg kg^{-1} (intraperitoneally injected). Tumor size was evaluated every 2 days, and the mice were euthanized upon reaching the endpoints, i.e., the tumor volume reached 2000 mm^3.

Statistical analysis

The data were presented as mean ± SEM. All statistical analyses were conducted using GraphPad Prism software 7.0 (GraphPad Software) and R software. Two-group comparisons were analyzed using a two-tailed Student's t-test, and one-way ANOVA with post hoc Tukey test was used when comparing more than two groups. The log-rank Mantel-Cox test was used to evaluate the survival differences in different groups. A significance level of $P < 0.05$ was considered statistically significant for all types of analyses.

Reporting summary

Further information on research design is available in the Nature Portfolio Reporting Summary linked to this article.

Data availability

The scRNA-seq data generated in this study have been deposited in the NCBI Gene Expression Omnibus (GEO) database under accession code GSE268619. The authors declare that all the data supporting the findings of this manuscript are available within the manuscript and Supplementary Information files. All data are available from the corresponding author upon request. Processed feature barcode matrices for all scRNAseq data are available through the Gene Expression Omnibus with accession number GSE268619. Source data are provided with this paper.

Code availability

No new software was developed during this study. The code used for processing scRNA-seq data sets is available at https://github.com/zbx2801/AIE-COF-induced-iTLS.

References

1. Hodi, F. S. et al. Improved survival with ipilimumab in patients with metastatic melanoma. *N. Engl. J. Med.* **363**, 711–723 (2010).
2. Morad, G. et al. Hallmarks of response, resistance, and toxicity to immune checkpoint blockade. *Cell* **184**, 5309–5337 (2021).
3. Ni, Q. et al. A bi-adjuvant nanovaccine that potentiates immunogenicity of neoantigen for combination immunotherapy of colorectal cancer. *Sci. Adv.* **6**, eaaw6071 (2020).
4. Pardoll, D. M. et al. The blockade of immune checkpoints in cancer immunotherapy. *Nat. Rev. Cancer* **12**, 252–264 (2012).
5. Sacco, A. G. et al. Pembrolizumab plus cetuximab in patients with recurrent or metastatic head and neck squamous cell carcinoma: an open-label, multi-arm, non-randomised, multicentre, phase 2 trial. *Lancet Oncol* **22**, 883–892 (2021).
6. Seiwert, T. Y. et al. Safety and clinical activity of pembrolizumab for treatment of recurrent or metastatic squamous cell carcinoma of the head and neck (KEYNOTE-012): an open-label, multicentre, phase 1b trial. *Lancet Oncol.* **17**, 956–965 (2016).
7. Helmink, B. A. et al. B cells and tertiary lymphoid structures promote immunotherapy response. *Nature* **577**, 549–555 (2020).
8. Petitprez, F. et al. B cells are associated with survival and immunotherapy response in sarcoma. *Nature* **577**, 556–560 (2020).
9. Cabrita, R. et al. Tertiary lymphoid structures improve immunotherapy and survival in melanoma. *Nature* **577**, 561–565 (2020).
10. Koscsó, B. et al. Gut-resident CX3CR1hi macrophages induce tertiary lymphoid structures and IgA response in situ. *Sci. Immunol.* **5**, eaax0062 (2020).
11. Schumacher, T. N. & Thommen, D. S. Tertiary lymphoid structures in cancer. *Science* **375**, eabf9419 (2022).
12. Derks, S. et al. Characterizing diversity in the tumor-immune microenvironment of distinct subclasses of gastroesophageal adenocarcinomas. *Ann. Oncol.* **31**, 1011–1020 (2020).
13. Sato, Y. Stem-like CD4+T cells in perivascular tertiary lymphoid structures sustain autoimmune vasculitis. *Sci. Transl. Med.* **15**, eadh0380 (2023).
14. Sautes-Fridman, C., Petitprez, F., Calderaro, J. & Fridman, W. H. Tertiary lymphoid structures in the era of cancer immunotherapy. *Nat. Rev. Cancer* **19**, 307–325 (2019).
15. Zhang, Y. et al. 3D printing scaffold vaccine for antitumor immunity. *Adv. Mater.* **33**, 2106768 (2021).

16. Jin, X.-K. et al. Engineering metal-based hydrogel-mediated tertiary lymphoid structure formation via activation of the STING pathway for enhanced immunotherapy. *Mater. Horiz.* **10**, 4365–4379 (2023).
17. Liu, C. et al. A nanovaccine for antigen self-presentation and immunosuppression reversal as a personalized cancer immunotherapy strategy. *Nat. Nanotechnol.* **17**, 531–540 (2022).
18. Han, X. et al. Adjuvant lipidoid-substituted lipid nanoparticles augment the immunogenicity of SARS-CoV-2 mRNA vaccines. *Nat. Nanotechnol.* **18**, 1105–1114 (2023).
19. Gong, N. et al. Proton-driven transformable nanovaccine for cancer immunotherapy. *Nat. Nanotechnol.* **15**, 1053–1064 (2020).
20. Xu, J. et al. A general strategy towards personalized nanovaccines based on fluoropolymers for post-surgical cancer immunotherapy. *Nat. Nanotechnol.* **15**, 1043–1052 (2020).
21. Theivendran, S., Lazarev, S. & Yu, C. Mesoporous silica/organosilica nanoparticles for cancer immunotherapy. *Exploration* **3**, 20220086 (2023).
22. Yang, K. et al. Zinc cyclic di-AMP nanoparticles target and suppress tumours via endothelial STING activation and tumour-associated macrophage reinvigoration. *Nat. Nanotechnol.* **17**, 1322–1331 (2022).
23. Dai, L. et al. Multifunctional metal-organic framework-based nanoreactor for starvation/oxidation improved indoleamine 2,3-dioxygenase-blockade tumor immunotherapy. *Nat. Commun.* **13**, 2688 (2022).
24. Asrir, A. et al. Tumor-associated high endothelial venules mediate lymphocyte entry into tumors and predict response to PD-1 plus CTLA-4 combination immunotherapy. *Cancer Cell* **40**, 318–334 (2022).
25. Diereks, C. S. & Yaghi, O. M. The atom, the molecule, and the covalent organic framework. *Science* **355**, 923–931 (2017).
26. Gao, P. A. et al. COF-based nanoplatform for highly efficient cancer diagnosis, photodynamic therapy and prognosis. *Chem. Sci.* **11**, 6882–6888 (2020).
27. Guan, Q. et al. A glycosylated covalent organic framework equipped with BODIPY and CaCO3 for synergistic tumor therapy. *Angew. Chem. Int. Ed.* **59**, 18042–18047 (2020).
28. Zhang, L. et al. Integration of AIEgens into covalent organic frameworks for pyroptosis and ferroptosis primed cancer immunotherapy. *Nat. Commun.* **14**, 5355 (2023).
29. Shi, Y. et al. Localized nuclear reaction breaks boron drug capsules loaded with immune adjuvants for cancer immunotherapy. *Nat. Commun.* **14**, 1884 (2023).
30. Sun, M. et al. Bioorthogonal-activated in situ vaccine mediated by a COF-based catalytic platform for potent cancer immunotherapy. *J. Am. Chem. Soc.* **145**, 5330–5341 (2023).
31. Wang, D. et al. Etching bulk covalent organic frameworks into nanoparticles of uniform and controllable size by the molecular exchange etching method for sonodynamic and immune combination antitumor therapy. *Adv. Mater.* **34**, 2205924 (2022).
32. Duan, Y. et al. Reticular chemistry-enabled sonodynamic activity of covalent organic frameworks for nanodynamic cancer therapy. *Angew. Chem. Int. Ed.* **62**, e202302146 (2023).
33. Zhang, L. et al. AIEgen-based covalent organic frameworks for preventing malignant ventricular arrhythmias via local hyperthermia therapy. *Adv. Mater.* **35**, 1700548–1700554 (2023).
34. Liu, S. et al. Construction of multiform hollow-structured covalent organic frameworks via a facile and universal strategy for enhanced sonodynamic cancer therapy. *Angew. Chem. Int. Ed.* **62**, e202301831 (2023).
35. Singh, N. et al. Nanoscale porous organic polymers for drug delivery and advanced cancer theranostics. *Chem. Soc. Rev.* **50**, 12883–12896 (2021).
36. Zhang, L. et al. Activation of pyroptosis using AIEgen-based sp^2 carbon-linked covalent organic frameworks. *J. Am. Chem. Soc.* **145**, 17689–17699 (2023).
37. Mitra, S. et al. Targeted drug delivery in covalent organic nanosheets (CONs) via sequential postsynthetic modification. *J. Am. Chem. Soc.* **139**, 4513–4520 (2017).
38. Zhang, L., Yi, L., Sun, Z.-J. & Deng, H. Covalent organic frameworks for optical applications. *Aggregate* **2**, e24–e37 (2021).
39. Luo, J. et al. Aggregation-induced emission of 1-methyl-1,2,3,4,5-pentaphenylsilole. *Chem. Commun.* **18**, 1740–1741 (2001).
40. Wu, W. et al. A highly efficient and photostable photosensitizer with near-infrared aggregation-induced emission for image-guided photodynamic anticancer therapy. *Adv. Mater.* **29**, 1700548–1700554 (2017).
41. Pham, T. C. et al. Recent strategies to develop innovative photosensitizers for enhanced photodynamic therapy. *Chem. Rev.* **121**, 13454–13619 (2021).
42. Ascherl, L. et al. Molecular docking sites designed for the generation of highly crystalline covalent organic frameworks. *Nat. Chem.* **8**, 310–316 (2016).
43. Qi, H. et al. Near-atomic-scale observation of grain boundaries in a layer-stacked two-dimensional polymer. *Sci. Adv.* **6**, eabb5976 (2020).
44. Pang, Z.-F. et al. Regulating the topology of 2D covalent organic frameworks by the rational introduction of substituents. *Chem. Sci.* **8**, 3866–3870 (2017).
45. Zhou, T.-Y. et al. One-step construction of two different kinds of pores in a 2D covalent organic framework. *J. Am. Chem. Soc.* **136**, 15885–15888 (2014).
46. Puram, S. V. et al. Single-cell transcriptomic analysis of primary and metastatic tumor ecosystems in head and neck cancer. *Cell* **171**, 1611–1624 (2017).
47. Azizi, E. et al. Single-cell map of diverse immune phenotypes in the breast tumor microenvironment. *Cell* **174**, 1293–1308 (2018).
48. Hwang, B., Lee, J. H. & Bang, D. Single-cell RNA sequencing technologies and bioinformatics pipelines. *Exp. Mol. Med.* **50**, 1–14 (2018).
49. He, C. et al. Combinatorial photothermal 3D-printing scaffold and checkpoint blockade inhibits growth/metastasis of breast cancer to bone and accelerates osteogenesis. *Adv. Funct. Mater.* **31**, 2006214 (2021).
50. Cheng, H.-B. et al. Assembly strategies of organic-based imaging agents for fluorescence and photoacoustic bioimaging applications. *Chem. Soc. Rev.* **49**, 21–31 (2020).
51. Yang, S. et al. More is better: acceptor engineering for constructing NIR-II AIEgens to boost multimodal phototheranostics. **145**, 22776–22787 (2023).
52. Zhang, T. et al. Mitochondria-targeting phototheranostics by aggregation-induced NIR-II emission luminogens: modulating intramolecular motion by electron acceptor engineering for multimodal synergistic therapy. *Adv. Funct. Mater.* **32**, 2110526 (2022).
53. Yan, D. et al. Donor/π-bridge manipulation for constructing a stable NIR-II aggregation induced emission luminogen with balanced phototheranostic performance. *Angew. Chem. Int. Ed.* **60**, 26769–26776 (2021).
54. Liu, L.-H. et al. A red light activatable multifunctional prodrug for image-guided photodynamic therapy and cascaded chemotherapy. *Adv. Funct. Mater.* **26**, 6257–6269 (2016).
55. Tanay, A. & Regev, A. Scaling single-cell genomics from phenomenology to mechanism. *Nature* **541**, 331–338 (2017).
56. Young, M. D. Single-cell transcriptomes from human kidneys reveal the cellular identity of renal tumors. *Science* **361**, 594 (2018).
57. Rodriguez, A. B. et al. Immune mechanisms orchestrate tertiary lymphoid structures in tumors via cancer-associated fibroblasts. *Cell Reports* **36**, 109422 (2021).
58. Pitzalis, C. Ectopic lymphoid-like structures in infection, cancer and autoimmunity. *Nat. Rev. Immunol.* **14**, 447–462 (2014).

59. Nagarsheth, N., Wicha, M. S. & Zou, W. Chemokines in the cancer microenvironment and their relevance in cancer immunotherapy. *Nat. Rev. Immunol.* **17**, 559–572 (2017).
60. Barone, F. et al. IL-22 regulates lymphoid chemokine production and assembly of tertiary lymphoid organs. *Proc. Natl. Acad. Sci. USA* **112**, 11024–11029 (2015).
61. Kröncke, R. et al. Human follicular dendritic cells and vascular cells produce interleukin-7: a potential role for interleukin-7 in the germinal center reaction. *Eur. J. Immunol.* **26**, 2541–2544 (1996).
62. Wang, Z. et al. Syngeneic animal models of tobacco-associated oral cancer reveal the activity of in situ anti-CTLA-4. *Nat. Commun.* **10**, 5546 (2019).
63. Wang, Z. et al. Disruption of the HER3-PI3K-mTOR oncogenic signaling axis and PD-1 blockade as a multimodal precision immunotherapy in head and neck cancer. *Nat Commun* **12**, 2383 (2021).
64. Saddawi-Konefka, R. et al. Lymphatic-preserving treatment sequencing with immune checkpoint inhibition unleashes cDC1-dependent antitumor immunity in HNSCC. *Nat Commun* **13**, 4298 (2022).
65. Mantovani, A. et al. Macrophage polarization: tumor-associated macrophages as a paradigm for polarized M2 mononuclear phagocytes. *Trends Immunol* **23**, 549–555 (2002).
66. Loyher, P.-L. et al. Macrophages of distinct origins contribute to tumor development in the lung. *J. Exp. Med.* **215**, 2536–2553 (2018).
67. Limagne, E. et al. MEK inhibition overcomes chemoimmunotherapy resistance by inducing CXCL10 in cancer cells. *Cancer Cell* **40**, 136–152 (2022).
68. Balkwill, F. Tumour necrosis factor and cancer. *Nat. Rev. Cancer.* **9**, 361–371 (2009).
69. Shen, J. et al. Anti-cancer therapy with TNFα and IFNγ: a comprehensive review. *Cell Prolif* **51**, e12441 (2018).
70. Randall, T. D. et al. Development of secondary lymphoid organs. *Annu. Rev. Immunol.* **26**, 627–650 (2008).
71. Luther, S. A. et al. Differing activities of homeostatic chemokines CCL19, CCL21, and CXCL12 in lymphocyte and dendritic cell recruitment and lymphoid neogenesis. *J. Immunol.* **169**, 424–433 (2002).
72. Yoshida, H. et al. Different cytokines induce surface lymphotoxin-alphabeta on IL-7 receptor-alpha cells that differentially engender lymph nodes and Peyer's patches. *Immunity* **17**, 823–833 (2002).
73. Takatsu, K. Cytokines involved in B-cell differentiation and their sites of action. *Proc. Soc. Exp. Biol. Med.* **215**, 121–133 (1997).
74. Nayar, S. et al. Immunofibroblasts are pivotal drivers of tertiary lymphoid structure formation and local pathology. *Proc. Natl. Acad. Sci. USA* **116**, 13490–13497 (2019).

Acknowledgements

This work is supported by the National Natural Science Foundation of China (82472818, 82273202 to Z.-J.S., 82002879 to L.Z., and 21788102 to B.Z.T.), the Research Grants Council of Hong Kong (16305320, 16306620, N-HKUST609/19 and C6014-20W to B.Z.T.), the Innovation and Technology Commission (ITC-CNERC14SC01 to B.Z.T.), Interdisciplinary Innovative Foundation of Wuhan University XNJC202303 (Z.-J.S.), the scientific and technological Innovation Team of Shanxi Province (2022TD-36 to H.-T.F.), and the Fundamental Research Funds for the Central Universities (2042022dx0003, 2042023kf0141 to Z.-J.S.). The authors would like to thank OE Biotech Co., Ltd. (Shanghai, China) for the scRNA-seq experiments performed at the Single Cell Core Facility, shanghai Kylpharm Co., Ltd. for the supply of ligand, Shiyanjia Lab (www.shiyanjia.com) for their XPS tests, Core Research Facilities of College of Chemistry and Molecular Sciences at Wuhan University for the solid-state NMR and TEM characterizations.

Author contributions

Z.-J.S., B.Z.T., and J.W.Y.L. conceived and designed the experiments. L.Z., B.Z., M.-J.Z., H.L., Q.-C.Y., Y.-T.L., A.S., Y.J. and S.W. performed the experiments. W.L. did the DFT calculations. L.Z., R.T.K.K., H.-T.F., and J.S. analyzed the data. L.Z., B.Z.T., Y.-T.L., Z.-J.S., and J.W.Y.L. wrote the manuscript. All authors have approved the final version of the manuscript.

Competing interests

The authors declare no competing interests.

Additional information

Supplementary information The online version contains supplementary material available at https://doi.org/10.1038/s41467-024-55430-4.

Correspondence and requests for materials should be addressed to Jacky W. Y. Lam, Ben Zhong Tang or Zhi-Jun Sun.

Peer review information *Nature Communications* thanks Robert Saddawi-Konefka, and the other, anonymous, reviewer(s) for their contribution to the peer review of this work. A peer review file is available.